

TESTING THE EVOLUTIONARY LINK BETWEEN TYPE 1 AND TYPE 2 QUASARS WITH MEASUREMENTS OF THE INTERSTELLAR MEDIUM

JINYI SHANGGUAN^{1,2} AND LUIS C. HO^{1,2}

¹*Kavli Institute for Astronomy and Astrophysics, Peking University, Beijing 100871, China*

²*Department of Astronomy, School of Physics, Peking University, Beijing 100871, China*

ABSTRACT

In a popular scenario for the coevolution of massive black holes and galaxies, major mergers of gas-rich galaxies fuel vigorous star formation and obscured (type 2) quasar activity until energy feedback from the active galactic nucleus clears away the gas and dust to reveal an unobscured (type 1) quasar. Under this scenario, the precursor type 2 quasars should be more gas-rich than their type 1 counterparts, and both types of quasars are expected to be gas-deficient relative to normal, star-forming galaxies of similar stellar mass. We test this evolutionary hypothesis by investigating the infrared ($\sim 1 - 500 \mu\text{m}$) spectral energy distribution of 86 optically selected $z < 0.5$ type 2 quasars, matched in redshift and [O III] luminosity to a comparison sample of type 1 quasars. Contrary to expectations, the gas content of the host galaxies of type 2 quasars is nearly indistinguishable from that of type 1 quasar hosts, and neither type exhibits the predicted deficit in gas relative to normal galaxies. The gas mass fraction of quasar hosts appears unaffected by the bolometric luminosity of the active nucleus, although their interstellar radiation field is preferentially higher than that of normal galaxies, potentially implicating active galactic nucleus heating of the large-scale galactic dust.

Keywords: galaxies: active — galaxies: ISM — galaxies: nuclei — galaxies: Seyfert — (galaxies:)
quasars: general — infrared: ISM

1. INTRODUCTION

Mergers of gas-rich galaxies, which lead to loss of angular momentum of the gas and gas inflows, are often invoked as the mechanism to trigger the most powerful active galactic nuclei (AGNs) and quasars (Heckman et al. 1986; Sanders et al. 1988; Jogee 2006), which are accompanied or immediately preceded by a powerful starburst (Hopkins et al. 2006). The complex, chaotic distribution of the dusty interstellar medium (ISM) during the early phases of the merger process results in highly obscured black hole growth. The most luminous AGNs activated during this period are likely “type 2 quasars” (QSO2s). Once the black hole reaches a sufficiently large mass, the AGN can clear the gas and dust and reveal itself as a type 1 quasar (QSO1; Hopkins et al. 2008). Quasar-mode AGN feedback injects significant energy into the host galaxy and quenches galaxy-wide star formation, explosively removing the cold ISM from the host galaxy (Silk & Rees 1998; Fabian 2012). This scenario also provides a natural explanation for the coevolution of the black hole and its host galaxy (Kormendy & Ho 2013), which is implicated by the observed tight correlation between the mass of the black hole and the mass and velocity dispersion of the stellar bulge (Magorrian et al. 1998; Gebhardt et al. 2000; Ferrarese & Merritt 2000). Alternatively, one might explain the observed differences between QSO1s and QSO2s simply through viewing angle-dependent obscuration by a small-scale dusty torus, following the traditional AGN “unified model” (Antonucci 1993) originally proposed for lower luminosity Seyfert galaxies.

There have been many attempts to observationally test the merger-driven model for AGN evolution, but the results are still controversial. On the one hand, the host galaxies of QSO1s and QSO2s appear to have a number of differences, including their star formation rates (e.g., Kim et al. 2006; Chen et al. 2015), ionized gas velocity fields (Greene et al. 2011), radio continuum properties (Lal & Ho 2010), and local environment (Villarreal & Korn 2014). The apparent differences between the host galaxies of the two quasar types suggest that they are intrinsically different. If so, the two quasar types are linked by an evolutionary connection instead of purely by viewing-angle orientation. On the other hand, unequivocal evidence for the role of mergers or interactions in triggering AGN activity remains elusive. While some studies find that the incidence of AGNs increases in close galaxy pairs (e.g., Silverman et al. 2011), especially those with decreasing physical separation (Ellison et al. 2011), others fail to find a clear enhancement of merger features in *Hubble Space Telescope* (*HST*) images of AGN and quasar host galaxies (e.g., Grogin et al.

2005; Cisternas et al. 2011; Kocevski et al. 2012; Böhm et al. 2013; Villforth et al. 2014; Mechtley et al. 2016; Villforth et al. 2017; Zhao et al. 2019). Such morphological studies, however, are subject to uncertainties due to image depth (Bennert et al. 2008; Hong et al. 2015), image contrast with the bright nucleus, time lag between galaxy coalescence and the onset of AGN activity (Böhm et al. 2013; Villforth et al. 2017), and possible biases stemming from X-ray sample selection (e.g., Kocevski et al. 2015; Shangguan et al. 2016).

The above studies largely focus on the stars of the host galaxy. The ISM component of the host provides complementary insights. The evolutionary scenario naturally predicts that QSO1 host galaxies should be more gas-deficient than QSO2 hosts as a result of efficient blow-out of cold gas by AGN feedback during the QSO1 phase. If AGN activity turns on with a substantial time delay (e.g., $\gtrsim 1$ Gyr) after the onset of starburst activity, we also expect quasar host galaxies (of either type) to have systematically reduced gas content compared to normal galaxies of similar stellar mass, even for star formation rates of relatively modest intensity (e.g., $\sim 10 M_{\odot} \text{ yr}^{-1}$). While observations of the CO molecule can probe molecular gas in AGNs over a wide range of redshifts and luminosities, from nearby lower luminosity sources (Scoville et al. 2003; Evans et al. 2006; Bertram et al. 2007; Husemann et al. 2017) to powerful quasars out to $z \gtrsim 6$ (e.g., Wang et al. 2013; Cicone et al. 2014; Walter et al. 2004; Wang et al. 2016), they are still quite time-consuming to make and plagued by uncertainty from the CO-to-H₂ conversion factor (Bolatto et al. 2013). In the mean time, H I observations currently can hardly extend beyond $z \approx 0.2$, where most quasars lie. Thanks to the unprecedented sensitivity and spatial resolution of the *Herschel Space Observatory* (Pilbratt et al. 2010), we can probe the cold ISM accurately and efficiently with dust emission in the far-infrared (FIR).

Shangguan et al. (2018) recently developed a new method to measure dust masses from detailed modeling of the IR spectral energy distribution (SED) of quasars, from which robust total (atomic and molecular) gas masses can be derived using gas-to-dust ratios estimated from the metallicity and the mass-metallicity relation. They applied their technique to study the ISM content of the sample of 87 $z < 0.5$ QSO1s from the Palomar-Green (PG; Schmidt & Green 1983) survey. Here we focus our attention on QSO2s, choosing a sample well-matched to the PG QSO1s, with the intent of investigating the possible evolutionary connection between these two types of luminous AGNs. We measure the dust masses of QSO2s from their photometric SEDs and estimate the total gas masses based on the dust

content, closely following the methodology developed for our previous study of QSO1s (Shangguan et al. 2018). We find that the hosts of QSO1s and QSO2s have surprisingly similar ISM properties. Both quasar types also turn out to have dust and gas fractions comparable to those of normal, star-forming galaxies of similar stellar mass. This result is in apparent conflict with the most basic expectation of the merger-driven evolutionary scenario for massive galaxies.

Luminous AGNs have diverse SEDs that may evolve with time (e.g., Haas et al. 2003). While it is beyond the scope of this work to sample the full range of luminous AGN properties, our study is designed to detect differences in gas mass between the two types of quasars, differences that are inevitable so long as quasar-mode feedback plays a critical role in transforming QSO2s to QSO1s. Our experiment probes the total cold gas content, not just the star-forming molecular medium as envisioned in the original evolutionary model of Sanders et al. (1988). Nevertheless, for AGN feedback to substantially influence galaxy evolution, it must affect the bulk of the cold ISM, which, in any event, is not distinguished into molecular or atomic phase in numerical simulations (e.g., Genel et al. 2014; Lagos et al. 2015). AGN outflows are widely regarded as multiphased (e.g., Harrison et al. 2018 and references therein).

The paper is organized as follows. Section 2 describes the quasar samples and data reduction to construct the near-IR (NIR) to FIR SED. The results of our measurements, including the stellar mass, interstellar radiation field intensity, and the dust and gas masses, are presented in Section 3. In Section 4, we investigate whether the differences between the SEDs of QSO1s and QSO2s can be explained by dust extinction and discuss the implications of our results in terms of the evolutionary scenario for quasars. This work adopts the following parameters for a Λ CDM cosmology: $\Omega_m = 0.308$, $\Omega_\Lambda = 0.692$, and $H_0 = 67.8 \text{ km s}^{-1} \text{ Mpc}^{-1}$ (Planck Collaboration et al. 2016).

2. SAMPLE AND DATA REDUCTION

2.1. Quasar Samples

Given our main goal of testing the hypothesis that QSO2s are the progenitors of QSO1s, we select closely matched samples of the two quasar types. Our reference sample of QSO1s are the 87 low-redshift ($z < 0.5$) optical/UV-selected PG quasars of Boroson & Green (1992), whose ISM properties are described in the companion paper by Shangguan et al. (2018). We choose 87 QSO2s (Table 1) derived from the Sloan Digital Sky Survey (SDSS; Reyes et al. 2008), randomly selected to match the PG QSO1s in both redshift and [O III]

$\lambda 5007$ luminosity (Figure 1). Following the earlier work of Zakamska et al. (2003), Reyes et al. (2008) identified QSO2s as extragalactic sources that have (1) optical diagnostic emission-line intensity ratios consistent with AGN excitation, (2) sufficiently narrow (FWHM $< 2000 \text{ km s}^{-1}$) permitted lines that make them likely candidates for type 2 sources, and (3) [O III] luminosities larger than $2 \times 10^8 L_\odot$, which, when translated to equivalent B -band absolute magnitudes, qualify them as quasars by the historical criterion of $M_B < -23 \text{ mag}$ (Schmidt & Green 1983). If an evolutionary link exists between the two types of quasars, we expect the gas masses of the QSO2 hosts to be systematically higher than those of the QSO1 hosts, for a given host galaxy stellar mass. Based on an X-ray study of QSO2s from our parent sample (Jia et al. 2013), we expect that more than half of our QSO2s are Compton-thick, and most of the rest of the objects should be considerably obscured.

For direct comparison with the QSO2s, we mainly focus on the subset of 55 QSO1s having stellar masses estimated from decomposition of high-resolution images (Zhang et al. 2016). Due to this additional constraint, the median properties of the two samples are slightly different, on average by ~ 0.2 dex in [O III] luminosity and ~ 0.03 dex in redshift, but the mismatch is small compared to the sample range and will not affect our conclusions.

Galaxy mergers play a role in triggering nuclear activity in the most powerful unobscured (Bahcall et al. 1997; McLure et al. 1999; Dunlop et al. 2003; Letawe et al. 2010; Hong et al. 2015) and obscured (Bessiere et al. 2012) quasars. Internal processes may be more relevant for activating nuclei of lower luminosity (Hopkins & Hernquist 2009; Treister et al. 2012; Villforth et al. 2017). Limitations in sensitivity and resolution make it very challenging to confirm whether any given host galaxy has experienced a merger, as tidal features can be faint and hard to detect, especially in the presence of an overpowering bright nucleus. Deep, ground-based imaging studies (Letawe et al. 2010; Hong et al. 2015) reveal a high incidence of tidal features and other morphological signatures suggestive of mergers in quasar host galaxies. We therefore work under the assumption that most of the quasars in our sample are triggered by mergers.

Part of our analysis will be restricted solely to the subset of QSO1s and QSO2s that are clearly hosted by galaxy mergers (Section 3.5). The information for QSO1s is mainly based on archival data (Kim et al. 2008, 2017) from *HST* and pointed observations from our own ongoing *HST* project (Y. Zhao et al., in preparation), supplemented by ground-based observations (Hong et al. 2015). One-third (29/87) of the QSO2s were observed

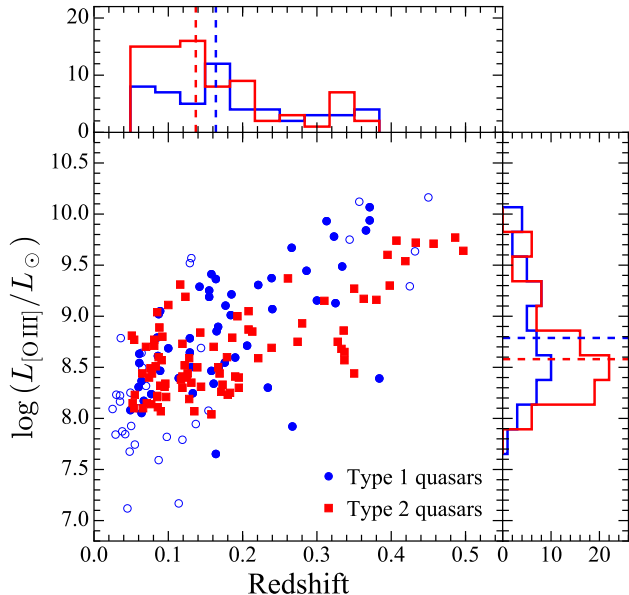


Figure 1. The distribution of redshift and [O III] $\lambda 5007$ luminosity of the samples of type 1 and type 2 quasars. The two samples are matched in terms of these two quantities. The filled blue circles are the type 1 quasars with host galaxy stellar mass measurements. We will use these objects to compare with the type 2 quasars, while the rest of the objects are in empty circles. The side panels show the distributions of the filled symbols of the type 1 and type 2 quasars. The dashed lines are the median values of the corresponding filled symbols. The type 1 quasars show on average ~ 0.2 dex higher [O III] luminosity and ~ 0.03 dex higher redshift, but these differences are small and unlikely to affect our results.

by our own *HST* project (Zhao et al. 2019), and the rest of the sample were examined with SDSS images, which, unfortunately, can hardly reveal galaxy merger features beyond $z \approx 0.15$. In total there are 11 QSO1s and 15 QSO2s with merger features at $z < 0.15$.

2.2. 2MASS and WISE

Emission from evolved stars of the host galaxy dominates the 2MASS (Skrutskie et al. 2006) *J* ($1.235 \mu\text{m}$), *H* ($1.662 \mu\text{m}$), and *K_s* ($2.159 \mu\text{m}$) bands (Cohen et al. 2003). We perform aperture photometry for the 2MASS data to obtain source flux densities or their respective upper limits. We collect the 2MASS images from the NASA/IPAC Infrared Science Archive (IRSA)¹ by matching each source with a $5''$ radius, and the measurements are conducted using the Python package *photutils*². We first fit and subtract the background

using a third-order two-dimensional polynomial function to remove possible large-scale gradients, mainly due to “airglow” emission (Jarrett et al. 2000). To measure the integrated flux of the source, we use the default aperture radius of $7''$ (Jarrett et al. 2000) with the sky annulus set to a radius of $25''$ to $35''$. For the nearest ($z \lesssim 0.1$) quasars with more extended host galaxies, we use larger aperture radii but the same sky annulus. However, larger aperture includes more noise. We, therefore, carefully choose the aperture radius ($10''$, $15''$, $20''$) to ensure that the flux of these extended sources is not below 3 times the uncertainty³. The selected apertures, which correspond to at least 12 kpc in physical size for our sample, are large enough to cover the entire galaxy. To determine the uncertainty, we perform 500 random aperture measurements of the sky, in exactly the same way as the quasar, with all sources masked, and calculate the standard deviation. We do not apply any aperture correction, which is found very small⁴. The measurements of eight targets are affected by projected close companions (see Table 2). We first use GALFIT (Peng et al. 2002, 2010) to fit and remove the companions from the images. The point-spread function (PSF) of each image is derived from the stars in the field using DAOPHOT in IRAF⁵ (Tody 1986). The residual (companion-subtracted) images are then measured using the same method described above. The measurements and the aperture radii are listed in Table 2.

In order to obtain accurate measurements that avoid the influence of projected companions, we also perform our own aperture photometry on the *WISE* images, following the method applied to the 2MASS data. We similarly collect *WISE* (Wright et al. 2010; Jarrett et al. 2011) *W1* ($3.353 \mu\text{m}$), *W2* ($4.603 \mu\text{m}$), *W3* ($11.561 \mu\text{m}$), and *W4* ($22.088 \mu\text{m}$) data from IRSA. We perform aperture photometry using “standard” aperture radii (Cutri et al. 2012) of $8''.25$ for the *W1*, *W2*, and *W3* bands and $16''.5$ for the *W4* band, adopting a sky annulus of $50''$ – $70''$. We use the curves of growth of coadded PSFs (Cutri et al. 2012) of the four *WISE* bands to calculate aperture correction factors. The uncertainty is also estimated by making 500 random measurements throughout the sky region. We carefully check the images and find 14 objects with close companions that show a flux

³ In contrast, we uniformly use a $20''$ aperture for the extended hosts of PG quasars (Shangguan et al. 2018) because they are all detected.

⁴ www.astro.caltech.edu/~jmc/2mass/v3/images/

⁵ IRAF is distributed by the National Optical Astronomy Observatories, which are operated by the Association of Universities for Research in Astronomy, Inc., under cooperative agreement with the National Science Foundation.

¹ irsa.ipac.caltech.edu/frontpage/

² <http://photutils.readthedocs.io/en/stable/>

density drop of more than 5% after we remove the companion(s) with GALFIT (Table 2). Due to the differences in wavelength and resolution, the projected companions in the *WISE* images are not necessarily the same as those in the 2MASS images. Although the resolution of the *WISE* images is low ($6''.1$, $6''.8$, $7''.4$, and $12''.0$ for *W1*, *W2*, *W3*, and *W4*, respectively), some objects with $z \lesssim 0.1$ tend to be marginally resolved in the first three *WISE* bands. We identify five objects whose flux densities increase by $\sim 20\% - 30\%$ when we measure with $20''$ aperture radius (Table 2). Due to the low resolution, a larger aperture is more likely to be contaminated by blended faint sources. We decide to keep the measurements with the $8''.25$ aperture radius, but enlarge the uncertainty of the *W1*–*W3* results to 30% of the flux densities. For the rest of the objects, mainly concerning those with $z \lesssim 0.1$, the $< 20\%$ flux decrease due to the small aperture will not affect our SED fitting. Both 2MASS (Jarrett et al. 2003) and *WISE* (Jarrett et al. 2011) have a calibration uncertainty of 3%; this is not included in Table 2. We note that our main statistical results are not affected by whether or not we include the objects with possibly larger uncertainty.

2.3. *Herschel*

The majority (84/87) of the QSO2 sample was observed by our own dedicated *Herschel* program (OT2_lho_2; PI: L. Ho) with both the Photodetector Array Camera and Spectrometer (PACS, Poglitsch et al. 2010) and the Spectral and Photometric Imaging Receiver (SPIRE, Griffin et al. 2010). The observation for one of the objects failed because of an error in the input coordinates. The remaining three sources were already observed by SPIRE by other programs (SDSS J0843+2944, KPOT_gsmith01.1, PI: T. Mueller; SDSS J1034+6001, SDP_soliver_3, PI: S. Oliver; SDSS J1218+0222, KPOT_jdavie01.1, PI: J. Davies). Thus, there are 86 objects with *Herschel* measurements, forming the QSO2 sample considered in this study.

We quote monochromatic flux densities at 70, 100, and 160 μm for PACS, and at 250, 350, and 500 μm for SPIRE (Table 3). The objects possibly affected by confusion from close companions, likely having larger uncertainties, are marked in the table. Our results, however, are not affected by whether or not these objects are included in the analysis. The standard pipeline assumes a constant νf_ν spectrum. We provide 3σ upper limits for non-detections. The calibration uncertainties for PACS and SPIRE photometry are both 5%, which are not included in the uncertainties quoted in Table 3. We do not apply a color correction but do consider the instrument spectral response functions in the SED modeling.

2.3.1. PACS

The QSO2 sample, like the PG QSO1s, is observed by PACS in mini-scan mode, with scan angles 70° and 110° and a scanning speed of $20''$ per second. PACS simultaneously scans the sources at short (70 or 100 μm) and long (160 μm) wavelengths over a field-of-view of $1'.75 \times 3'.5$. The integration time for each scan angle is 180 s.

The data are processed within version 15.0.1 of the Herschel Interactive Processing Environment (HIPE; Ott 2010), using the latest calibration files (calibration tree version 78). We use the script “Scanmap Pointsources PhotProject” provided by HIPE to reduce the timeline (level1) data into science images. In order to generate a proper mask for the high-pass filtering process to remove the “ $1/f$ noise”, a S/N-based mask is first generated. All the pixels above the 3σ threshold are masked. Then, a circular mask with `radius = 25''` is added at the nominal position of the target. The scan maps with different scan directions are drizzle-combined with the `photProject` function, using the default pixel fraction (`pixfrac = 1.0`) and reduced output pixel size of $1''.1$, $1''.4$, and $2''.1$ for the three bands, respectively. A smaller pixel fraction can, in principle, reduce the covariance noise, but we find that the noise does not significantly change when we set `pixfrac = 0.6`. The key parameters, described above, follow those used by Balog et al. (2014; their Section 4.1).

The flux density of the compact sources can be measured from aperture photometry with the aperture sizes and annulus radii for background subtraction following the recommendations of the *Herschel* Webinar “Photometry Guidelines for PACS data” by Paladini⁶. The aperture radii for bright sources are $12''$, $12''$, and $22''$ for 70, 100, and 160 μm bands, respectively, and the corresponding values for faint sources are $5''.5$, $5''.6$, and $10''.5$. The inner and outer radius of the sky annulus are $35''$ and $45''$, out to which the sky measurements are affected by the PSF wings less than 0.1% (Balog et al. 2014). Aperture correction is always necessary because the PSFs of PACS maps are very extended (see Table 2 of Balog et al. 2014).

As our quasars span redshifts $\sim 0.05 - 0.5$ with some displaying extended tidal features, it is important to carefully assess whether the aperture is large enough to enclose all the extended emission belonging to the targets, especially for the low- z objects. In order to determine the aperture radius for PG QSO1s in a similar

⁶ https://nhscsci.ipac.caltech.edu/workshop/Workshop_Oct2014/Photometry/PACS/PACS_phot_Oct2014_photometry.pdf

redshift range, [Shangguan et al. \(2018\)](#) find that objects fainter than 200 mJy at 100 μm can be measured with relatively small aperture radii (5''5, 5''6, and 10''5 for 70, 100, and 160 μm , respectively), while brighter objects should be measured with larger aperture radii (12'', 12'', and 22'' for 70, 100, and 160 μm , respectively). The larger apertures are usually big enough to accurately measure the partially resolved objects, even for $z < 0.05$, at the same time still able to avoid contaminating sources and minimize noise. For highly resolved objects, they chose to use more extended apertures of radii 18'', 18'', and 30'' for 70, 100, and 160 μm , respectively. The same method is used to determine the aperture of the QSO2s. Since SDSS images are available for the entire sample, we further examine the optical sizes of the sources. We extract and compare their flux densities using the small, large, and, if necessary, extended aperture. Only a few objects in our sample need to be measured with larger apertures. For example, SDSS J1200+3147 and SDSS J1238+6703 are ongoing mergers whose gas distributions are likely to be complex and distributed on multiple scales. For most of the objects, the variation of flux density as a function of different aperture sizes is always consistent within $1-2\sigma$ of the sky variation, proving that the aperture sizes are properly determined. The listed flux densities account for contamination by companions, as described below. To determine the uncertainties of the targets, we perform 20 measurements, centering the apertures evenly on the background annulus (with radius 45'') without background subtraction. The aperture sizes are exactly the same as those used to measure the sources. The standard deviation of the 20 measurements constitutes the 1σ uncertainty of the aperture photometry of the source ([Balog et al. 2014](#); [Shangguan et al. 2018](#)).

A few quasars have bright, close companions, which need to be removed to minimize their contamination. We again use GALFIT to simultaneously deblend the sources and companions. In order to generate the PSF for GALFIT, we use the observations of α Tau (obsid: 1342183538 and 1342183541; [Balog et al. 2014](#)), which we reprocessed with the same parameters as the quasars. Visual examination of the residual images show that the companions are very well removed from the images. Aperture photometry for the targets is performed on the residual images with the companions removed. Comparing the aperture photometry before and after companion removal, we find that the extracted flux densities of 10 quasars⁷ are affected by $> 5\%$. We only adopt

the measurements from the contamination-decomposed maps for the 10 objects with the corresponding bands (marked in Table 3), since the deviation is higher than the calibration uncertainty (5%). SDSS J0753+3847, at $z < 0.1$, is well-resolved, and its photometry is measured using the extended aperture. SDSS J0936+5924 resides in a complex region. It has at least one physical companion at $z \approx 0.096$, and a group of galaxies at $z \approx 0.04$ is projected against it. Since the center of the aperture cannot be reliably determined by fitting the source with a Gaussian profile in the companion-subtracted maps, we fix the center to the nominal optical position. Weak, extended emission may be present at 70 μm . We use a large aperture to enclose all the probable emission, even at the expense of incurring larger noise. SDSSJ1356+4304, like SDSS J0936+5924, also has a poorly determined centroid after companion deblending; we fix the center of the aperture but use a small aperture. The aperture for the rest of the objects, as for the main sample, is based on their 100 μm flux density.

2.3.2. SPIRE

The SPIRE imaging photometer ([Griffin et al. 2010](#)) covers a field-of-view of $4' \times 8'$ with a FWHM resolution of 18''1, 25''2, and 36''6 for the 250, 350, and 500 μm bands, respectively. The observations were conducted in the small-scan-map mode, with a single repetition scan for each object and a total on-source integration time of 37 s.

Data reduction was performed using HIPE (version 15.0.1; calibration tree `spire_cal_14_3`), following pipeline procedures to reduce the small maps. Although there are several bright targets, many of our sources are faint ($\lesssim 30$ mJy) and even undetected. Following the suggested strategy of photometry for SPIRE, we choose the HIPE build-in source extractor `Sussextractor` ([Savage & Oliver 2007](#)) to measure the positions and flux densities of the sources, with the error map generated from the pipeline and adopting a 3σ threshold for the detection limit. We measure the source within the FWHM of the beam around the nominal position of the quasar. For the three objects observed by other programs, we measure SDSS J0843+2944 and SDSS J1034+6001 with the same method. SDSS J1218+0222 is located on the edge of the map, so we use the measurements from the *Herschel*/SPIRE Point Source Catalog (HSPSC; [Schulz et al. 2017](#)). We quote the flux densities and un-

⁷ SDSS J0753+3847, J0936+5924, and J1356+4304 are contaminated in all three PACS bands. SDSS J1002+0551, J1022+4734,

J1101+4004, J1356+4259, J1405+4026, J1450-0106, and J1605+0742 are contaminated in the 160 μm band.

certainties provided by the SUSSEX source extractor. Following Leipski et al. (2014), we use the pixel-to-pixel fluctuations of the source-subtracted residual map to determine the uncertainty of the flux measurements. The residual map is created by subtracting all sources found by the source extractor from the observed map with 3σ threshold. We then calculate the pixel-to-pixel RMS in a box of size 8 times the beam FWHM of each band. The box size is large enough to include a sufficient number of pixels for robust statistics, but small enough to avoid the low-sensitivity area at the edges of the map. The median values of the RMS are 10.66, 9.18, and 11.29 mJy at 250, 350, and 500 μm , respectively. Leipski et al. (2014) found that this method tends to obtain uncertainties very close to, but a bit smaller than, those calculated from the quadrature sum of the confusion noise limit and the instrument noise (Nguyen et al. 2010). With a single repetition scan, the expected noise level is 10.71, 9.79, and 12.76 mJy at 250, 350, and 500 μm , respectively, very close to our actual measurements. We provide 3σ upper limits for all non-detections. Sources with flux densities below 3 times the RMS, even if detected by the source extractor, are considered non-detections.

We visually check the SDSS and PACS images to identify the sources that may be contaminated by close companions in the SPIRE maps due to poor resolution⁸. Except for those undetected in the SPIRE bands, the following objects are possibly contaminated: SDSS J0753+3847, J1102+6459, J1109+4233, J1258+5239, J1356+4259, J1356+1026, J1358+4741, and J1405+4026. The potentially contaminated measurements are marked in Table 3. However, since the companion sources are always much fainter than the quasar in PACS maps, we believe that the contamination is not significant. SDSS J1605+0742 is falsely detected at 500 μm because it is undetected at shorter wavelengths with higher resolution and comparable sensitivity.

3. RESULTS

3.1. Stellar Mass

The stellar mass is derived from the J -band photometry with a mass-to-light ratio (M/L) constrained by the $B - I$ color, following (Bell & de Jong 2001)

$$\log(M_*/M_\odot) = -0.4(M_J - M_{J,\odot}) - 0.75 + 0.34(B - I), \quad (1)$$

⁸ The FWHM of the beam is $18''1$, $25''2$, and $36''6$ at 250, 350, and 500 μm , respectively.

where M_J and $M_{J,\odot} = 3.65$ (Blanton & Roweis 2007) are the rest-frame J -band absolute magnitudes of the galaxy stellar emission and the Sun, respectively. The initial mass function (IMF) is converted from the scaled Salpeter (1955) IMF to the Chabrier (2003) IMF by subtracting 0.15 dex (Bell et al. 2003)⁹. We calculate M_J in two steps. First, the original J -band flux is subtracted by the emission from the AGN dust torus, following the results of the SED fitting (Section 3.2.2). Then, K-correction is applied based on a 5 Gyr simple stellar population model (Bruzual & Charlot 2003) assuming solar metallicity and a Chabrier (2003) IMF. The uncertainty of the K-correction, considering the uncertainty of the star formation history, is ~ 0.2 mag. We adopt a constant color, $B - I = 1.7$ mag, which is typical of the QSO2s in our sample Zhao et al. (2019). The uncertainty of the color-based stellar mass is assumed 0.2 dex (Conroy 2013). The results are listed in Table 1. As a cross check on our stellar masses, we compare our values with those for the 48 objects listed in common in the MPA/JHU catalog¹⁰ based on analysis of SDSS optical spectra; the two sets of measurements are consistent within a scatter of ~ 0.18 dex, close to our assumed uncertainty. The stellar masses of QSO2s span $M_* \approx 10^{10.3} - 10^{11.8} M_\odot$. The stellar masses of QSO1s are estimated from high-resolution optical and near-IR images (Zhang et al. 2016), assuming a mass-to-light ratio based on Bell et al. (2003). We convert the results based on the Salpeter IMF to the Chabrier IMF by scaling the stellar mass by a factor of 1.5 (Zhang et al. 2016). The uncertainties of the host galaxy stellar masses for QSO1s are likely larger than 0.2 dex, mainly due to contamination by the bright nuclei of QSO1s. Nevertheless, as shown in Section 3.5, the median stellar masses of the two groups are very similar. This suggests that the uncertainties of the stellar masses of QSO1s are not likely systematic.

3.2. SED Fitting

3.2.1. Models

The IR SED of quasars consists of stellar emission, AGN-heated dust (e.g., torus) emission, and cold dust emission on galactic scales. We fit the SED with a Bayesian Markov chain Monte Carlo (MCMC) method. We refer to Shanguan et al. (2018) for the details of the fitting method as well as the models for the stel-

⁹ Bell et al. (2003) provide the conversion from Salpeter IMF to Kroupa et al. (1993) IMF, which is close enough with the conversion to Chabrier (2003) IMF (e.g., Madau & Dickinson 2014).

¹⁰ <http://wwwmpa.mpa-garching.mpg.de/SDSS/DR7/Data/stellarmass.html>

lar (BC03) and cold dust (Draine & Li 2007; DL07) emission. The FIR emission of the torus drops rapidly beyond $\sim 20 \mu\text{m}$ (Lyu & Rieke 2017). As the cold dust of the large-scale ISM, which dominates the dust mass, emanates mainly at $\gtrsim 70 \mu\text{m}$, cold dust masses can be measured robustly using the DL07 model (Vito et al. 2014; Shangguan et al. 2018). We adopt a new version of the CAT3D model (Hönig & Kishimoto 2017) to fit the AGN dust torus emission. This model considers the different sublimation temperature of silicate and graphite dust, allowing the model to provide self-consistently more emission from the hot dust at the inner edge of the torus. This inner, hot component had been modeled as an additional blackbody component in previous models such as CLUMPY (Nenkova et al. 2008a,b), as well as in the earlier version of CAT3D (Hönig & Kishimoto 2010). García-González et al. (2017) also recently provide a new set of torus templates based on the CAT3D model. In Appendix B, we compare the SED fitting with the two new sets of CAT3D torus models, along side the median CLUMPY template obtained from PG quasars (Shangguan et al. 2018). We find that the choice of the torus model has little, if any, effect on the measurements of cold dust properties (Shangguan et al. 2018; Zhuang et al. 2018). We choose to use the results based on the templates of Hönig & Kishimoto (2017), as they provide the best overall fits. The SEDs for the QSO1s have the advantage of including *Spitzer* mid-IR (MIR) spectra, but, fortunately, the cold dust masses are not compromised by the use of purely photometry-based SEDs (Shangguan et al. 2018). Although an optional polar wind component is available for the torus templates (Hönig & Kishimoto 2017), we choose the templates without a wind component because they suffice to fit the MIR *WISE* data, at the same time avoiding the need to introduce several additional, poorly constrained free parameters. None of the QSO2s in our sample exhibits obvious signs of jet radiation in the *Herschel* bands from radio-loud sources; therefore, synchrotron emission is not included in any of the fits. The parameters and priors for the three model components are summarized in Table 4.

3.2.2. Fitting Results

As shown in Figure 2, most of the QSO2 SEDs can be reasonably well fitted by our combined model. With more than four bands detected in *Herschel*, at least half of the sample can be fitted well because the peak of the FIR SED is well-constrained by the data (Figure 2a). Even with fewer *Herschel* bands detected, it is still possible to constrain the DL07 model, albeit with relatively large uncertainty (Figures 2b and 2c), unless the upper limit at $250 \mu\text{m}$ is effectively low. There are 14 ob-

jects detected by *Herschel* with $\lesssim 2$ bands (e.g., Figure 2d). It is impossible to constrain the DL07 model for these; instead, the DL07 model, if set free, will mainly fit the mismatch of the torus component. Therefore, we fix $U_{\text{min}} = 1.0$ and manually adjust M_d in steps of 0.1 dex to estimate an upper limit on the dust mass. Given the same flux, a lower U_{min} corresponds to a higher M_d . Note that $U_{\text{min}} = 1$ is the interstellar radiation field in the solar neighborhood, which is not likely higher than that in a quasar host galaxy. Therefore, we believe that this is a reasonable assumption to estimate upper limits for the dust mass.

The torus component of QSO2s is usually much less prominent than that of QSO1s, mainly because the hot dust emission in the NIR suffers stronger extinction in obscured AGNs, regardless of where the obscuration comes from. Interestingly, five objects¹¹ show strong hot dust emission in the NIR, even prominent enough to dominate over the stellar component (e.g., Figure 2b). This diversity of MIR SEDs is consistent with the analysis of Hiner et al. (2009). The fitting results are listed in Table 1.

3.3. ISM Radiation Field

The physical parameter U_{min} probes the intensity of the interstellar radiation field. Figure 3a shows the distribution of U_{min} for QSO2s, comparing them with QSO1s as well as normal galaxies from the KINGFISH survey (Draine et al. 2007; Kennicutt et al. 2011) and the *Herschel* Reference Survey (HRS; Boselli et al. 2010; Ciesla et al. 2014). It is clear that the distributions for the host galaxies of *both* quasar types follow a similar trend, rising toward high U_{min} , while normal galaxies follow the opposite tendency, peaking at low values of U_{min} . The large values of U_{min} likely indicate that the spatial distribution of the ISM in both types of quasars is highly concentrated. Furthermore, U_{min} increases with increasing AGN strength (here taken to be $L_{[\text{O III}]}$, the luminosity of the [O III] $\lambda 5007$ line; Figure 3b). This is consistent with the results from Shangguan et al. (2018), where U_{min} for PG quasars also shows a similar general trend with increasing AGN continuum luminosity $\lambda L_{\lambda}(5100 \text{ \AA})$. The physical mechanism driving this correlation is unclear. As discussed in Shangguan et al. (2018), it might arise from AGN heating of dust in the narrow-line region. Whatever the exact physical origin, the apparent contribution of AGN heating to the FIR emission suggests that caution must be exercised in

¹¹ SDSS J0843+2944, J0858+3121, J1100+0846, J1316+4452, and J1641+4321.

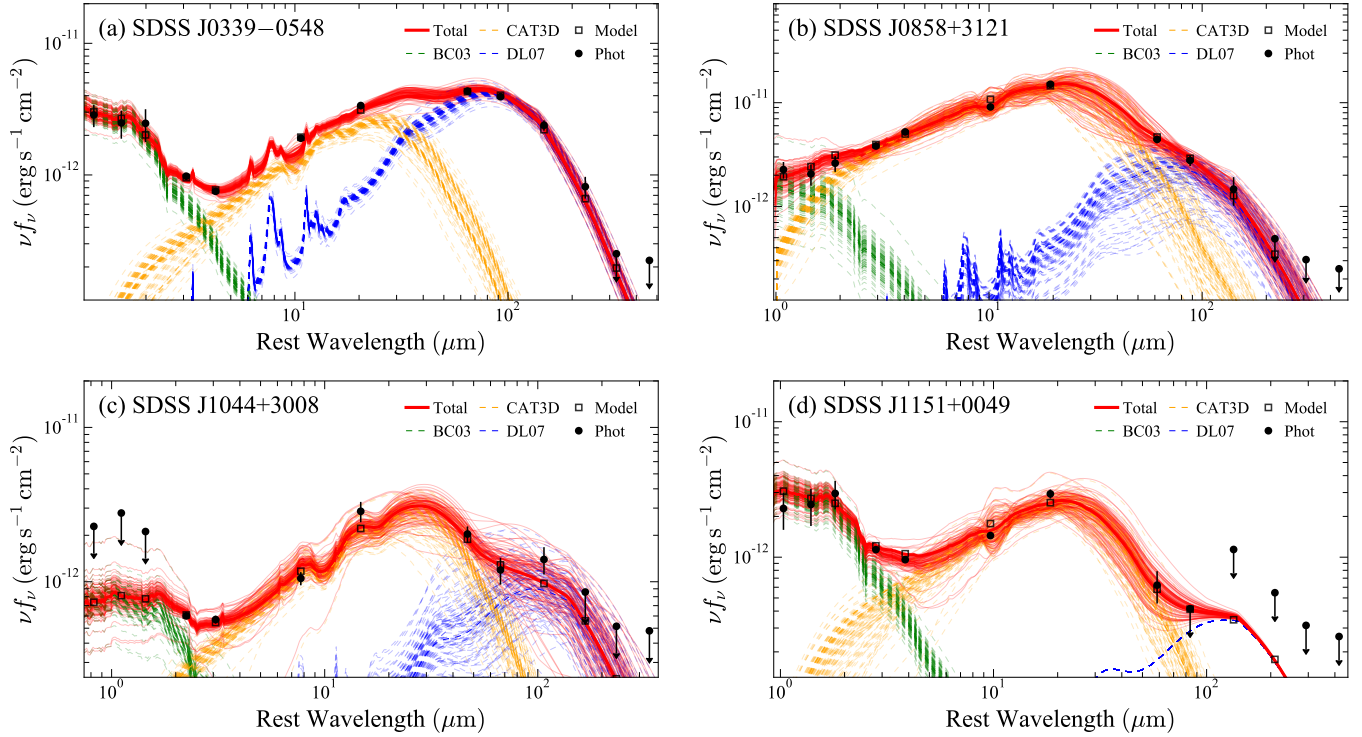


Figure 2. Four examples of SED fitting results for QSO2s. The black points are the photometric data from 2MASS, *WISE*, and *Herschel*. The dashed lines are the individual components for stars (green; BC03), torus (orange; CAT3D), and host galaxy dust (blue; DL07). The combined best-fit model is plotted as a red solid line. To visualize the model uncertainties, the associated thin lines represent 100 sets of models with parameters drawn randomly from the space sampled by the MCMC algorithm. With detections in four *Herschel* bands, SDSS J0339–0548 (a) has a very well-constrained model. The fitting for SDSS J0858+3121 (b) is also reasonably good, because the upper limits provide meaningful constraints on the peak of the FIR SED. SDSS J1044+3008 (c) is only detected in the *Herschel* PACS bands, and thus the uncertainty of the DL07 component is significant. For SDSS J1151+0049 (d), the FIR data are even less constraining, and the DL07 component cannot be fit freely. We fix $U_{\min} = 1.0$ and manually adjust the amplitude of the DL07 component to estimate an upper limit on M_d . The best-fit results for the entire sample of 86 objects can be found in the online version.

ascribing all the FIR emission to star formation, as is customary in the literature.

3.4. ISM Mass

We convert the dust masses, derived from the SED fitting, to total gas masses following the method developed by Shanguan et al. (2018):

$$M_{\text{gas}} = M_{\text{HI}} + M_{\text{H}_2} = M_d \delta_{\text{GDR, total}}, \quad (2)$$

$$\log \delta_{\text{GDR, total}} = \log \delta_{\text{GDR}} + (0.23 \pm 0.03), \quad (3)$$

where $\delta_{\text{GDR, total}}$ is the gas-to-dust ratio (δ_{GDR}) estimated from the galaxy stellar mass and corrected to account for the extended HI gas in the outskirts of the galaxy. We estimate δ_{GDR} from the galaxy stellar mass, combining the mass-metallicity relation (M_*-Z ; Kewley & Ellison 2008) and the δ_{GDR} -metallicity relation

($\delta_{\text{GDR}}-Z$; Magdis et al. 2012).¹² The values of δ_{GDR} for the objects with measured stellar masses lie in the range $\sim 121 - 145$, with a median of 122 ± 6 , similar to those of QSO1s reported in Shanguan et al. (2018). We adopt the median δ_{GDR} from the stellar mass-detected objects for those whose stellar masses only have upper limits. Since the uncertainty on δ_{GDR} is ~ 0.2 dex, this will not introduce significantly more uncertainty to the gas masses of the objects without stellar mass measurements (usually more distant). The dust and gas masses of QSO2 host galaxies lie in the range $10^{6.7} - 10^{8.9} M_{\odot}$ and $10^{8.8} - 10^{11.0} M_{\odot}$, respectively (Table 1). These photometry-based ISM masses of QSO2s can be directly compared to those of QSO1s, as the additional benefit of *Spitzer* spectra enjoyed by the latter matters little for the dust masses (Shanguan et al. 2018).

¹² See Equations (15) and (16) in Shanguan et al. (2018).

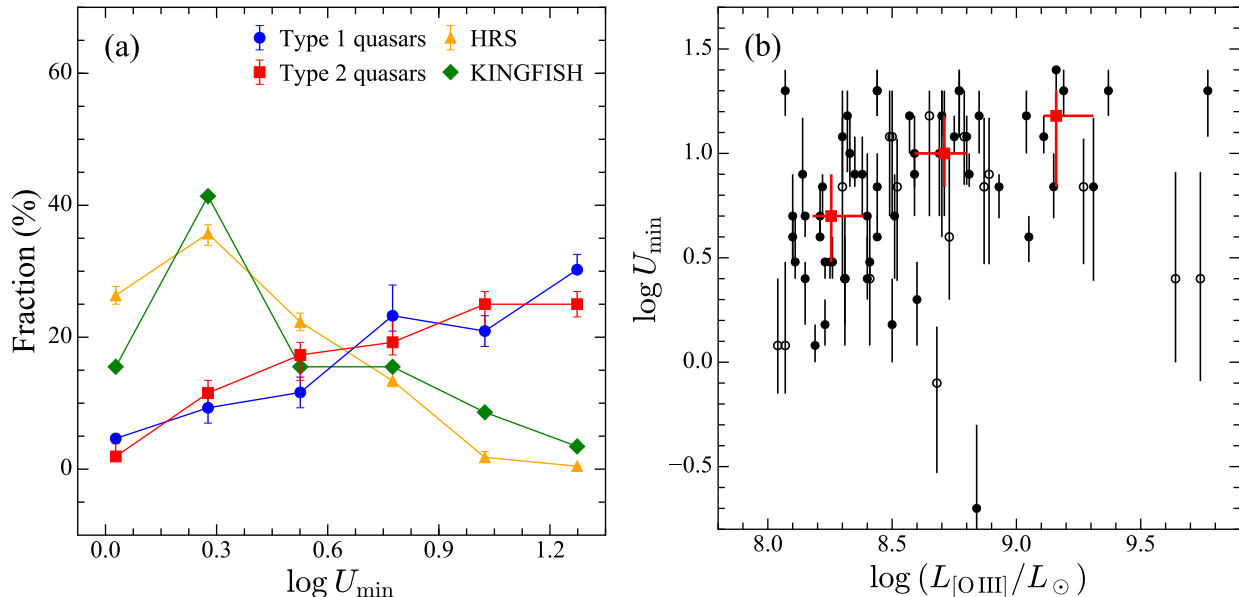


Figure 3. The dust-probed interstellar radiation field. (a) Distribution of U_{\min} for type 1 quasars (blue circles), type 2 quasars (red squares), and normal galaxies from the KINGFISH (green diamonds) and HRS (orange triangles) samples. The errors for the quasars and HRS galaxies are estimated with a Monte Carlo method, resampling the parameters according to their measured errors and calculating the number of galaxies in each bin for 500 times. The error bars represent 25th–75th percentile ranges of the resampled distribution in each bin. Since measurement errors of the KINGFISH galaxies are not available, no error bars are associated with the green diamonds. The star-forming and quenched galaxies in the KINGFISH and HRS samples peak at low U_{\min} . By contrast, the host galaxies of both types of quasars tend to have higher U_{\min} . (b) The values of U_{\min} for type 2 quasars generally increase with increasing [O III] luminosity. The filled circles represent more robust measurements than the open circles; we omitted objects for which only upper limits are available for the dust mass. To better visualize the observational trend, we grouped the sample into three bins: $\log L_{[\text{O III}]} < 8.5$, $8.5-9.0$, and $\gtrsim 9.0$; the 50 $^{+25}_{-25}$ th percentile of the distribution in each bin is plotted as red squares with error bars.

3.5. Comparison of Gas Masses of Quasars and Galaxies

As shown in Figure 4, the gas content of QSO1s strongly overlaps with that of QSO2s, and both quasar types possess comparable amounts of ISM as normal, star-forming galaxies of the same stellar mass.¹³ It is clear that the median values of the quasars are very close to the median value of the normal galaxies within ± 0.4 dex (Chang et al. 2015) around the star-forming main sequence derived by Saintonge et al. (2016). Meanwhile, quasars are more gas-rich than the entire normal galaxy sample, in which many gas-poor systems with quenched star formation are included, consistent with Vito et al. (2014). The similarity of the cold ISM content of the two quasar populations is further reinforced by the close resemblance of their median FIR SEDs (see Section 4.1). The quasars hosted by galaxy mergers that clearly dis-

play tidal features (see Section 2.1) do not show significant difference in gas and stellar mass distribution compared to the rest of the sample. Note that the same conclusions are obtained by comparing the dust mass of quasars with that of normal galaxies in the HRS sample, although the number of objects with $M_* > 10^{10.5} M_{\odot}$ is relatively small.

Sanders et al. (1988) proposed that gas-rich major mergers produce ultraluminous IR galaxies, which then evolve into QSO1s after the gas and dust are cleared. While ISM masses exist for local luminous and ultraluminous IR galaxies (e.g., Shangguan et al. 2019), comparing them to those of quasars is fraught with difficulty because IR-selected galaxies are biased toward dusty, and hence gas-rich, objects. Nevertheless, we note that more than 60% of our QSO2s have total IR (8–1000 μm) luminosities in excess of $10^{11} L_{\odot}$.

We employ survival analysis as implemented in the IRAF.ASURV package (Feigelson & Nelson 1985) to include the upper limits of dust, gas, and stellar masses in the statistical comparisons. Specifically, we use the Kaplan-Meier product limit estimator (`kmestimate`

¹³ The star-forming galaxies are from the xCOLD GASS survey (Saintonge et al. 2017), a representative, mass-selected ($M_* > 10^9 M_{\odot}$) sample of 532 local ($0.01 < z < 0.05$) galaxies with both CO(1–0) and H I measurements.

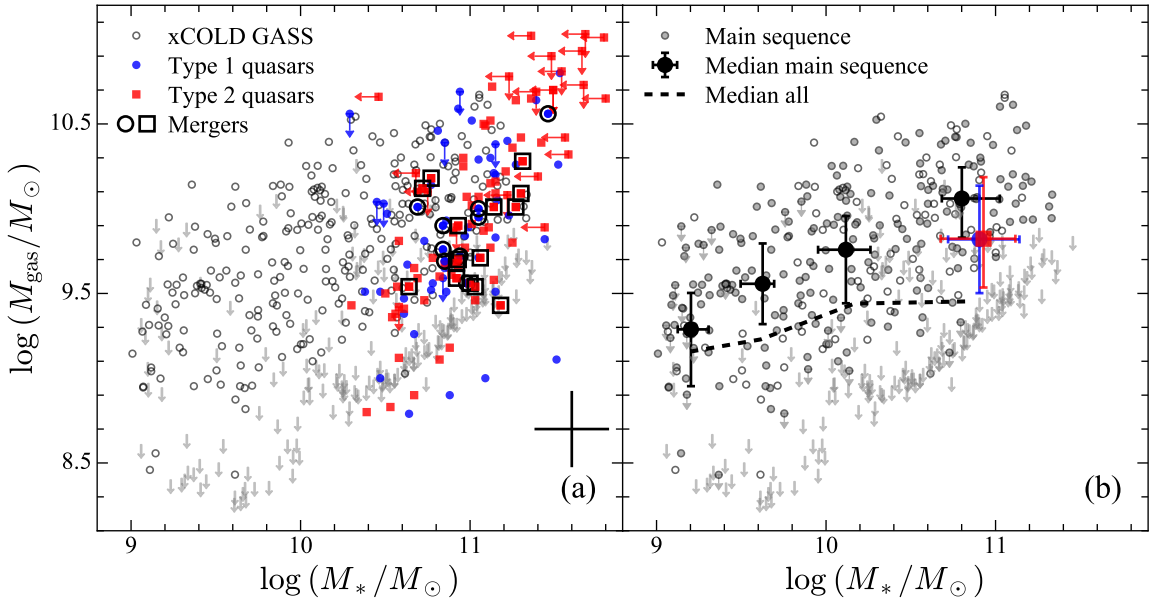


Figure 4. The gas and stellar masses of quasars compared to those normal galaxies. The individual objects are plotted in (a), while the medians of the quasars and normal galaxies are shown in (b). Type 2 quasars (red squares) display similar distributions of M_{gas} and M_* as type 1 quasars (blue circles), and both quasar types resemble star-forming galaxies (grey circles). Median gas and stellar masses of the two quasar types are very similar. They are also consistent with those of the normal galaxies on the main sequence (individual objects: filled gray circles; median: large black circles). The possible differences between the median gas mass and stellar mass of quasars and main-sequence galaxies in the most massive bin are well within the error bars. Meanwhile, quasars show higher gas masses compared to the median of all the normal galaxies (dashed line), as many gas-poor galaxies are included. Quasars at $z < 0.15$ involved in a galaxy merger [large empty circles and squares in (a)] do not stand out in any particular way. The error bars in (a) illustrate the typical uncertainty of the gas and stellar masses for the quasars. The error bars in (b) represent the 25th–75th percentile ranges of the sample distribution.

task) to calculate the 50_{-25}^{+25} th percentile of each physical quantity. The median and ± 25 percentiles of the two quasar types are very similar for all the masses (dust, gas, and stars). In order to consider measurement uncertainties, we use a Monte Carlo method to resample the dust, gas, and stellar masses 500 times assuming Gaussian distributions with the mean and dispersion following the measured values and uncertainties. We then use the Kaplan-Meier estimator to calculate the medians of the resampled data. The two types of quasars remain very similar when uncertainties are considered (Table 5). For the subsamples of quasars hosted by mergers at $z < 0.15$, the median gas and stellar masses of QSO1s are $10^{9.74}$ and $10^{10.94} M_{\odot}$, while those of QSO2s are $10^{9.71}$ and $10^{10.97} M_{\odot}$. The differences between QSO1s and QSO2s are small and statistically indistinguishable for the merger-matched subsamples. The differences between the merger subsamples and the whole quasar samples are also small.

Furthermore, we also use the `twosampt` task to test the null hypothesis that the dust, gas, and stellar masses of the two types of quasars are drawn from the same parent distribution. The probabilities of the null hy-

pothesis are 52.4%, 59.2%, and 95.1%, respectively, for dust, gas, and stellar masses. We also use the Monte Carlo method to generate 500 resampled datasets and repeat the two-sample test. The 50_{-25}^{+25} th percentiles of the probability of the null hypothesis are $44.7_{-18.2}^{+24.5}\%$, $48.3_{-22.6}^{+25.6}\%$, and $57.5_{-21.2}^{+19.9}\%$, respectively. Therefore, we cannot rule out the null hypothesis that QSO1s and QSO2s are drawn from the same parent distribution. We only report the results from the Peto-Prentice generalized Wilcoxon test, as suggested by Feigelson & Nelson (1985); the results from the other methods implemented by the task are entirely consistent.

The Kaplan-Meier estimator is also used to calculate the 50_{-25}^{+25} th percentile of the gas and stellar masses of the normal galaxies, as well as the main-sequence subsample thereof. For the main-sequence galaxies, only a small fraction of the gas masses are upper limits, so the results from the Kaplan-Meier estimator are robust. However, there are too many upper limits for the gas masses to estimate the lower end of the distribution for the overall sample, so that we only plot the median values (dashed line) in Figure 4b. We divide the normal galaxies into four stellar mass bins: $M_* < 10^{9.4}$,

$10^{9.4} - 10^{9.8}$, $10^{9.8} - 10^{10.5}$, and $> 10^{10.5} M_{\odot}$, ensuring that there are enough objects in each bin for robust statistics. The main-sequence galaxies in the last mass bin ($M_* > 10^{10.5} M_{\odot}$) show gas and stellar masses consistent with those of the quasars.

4. DISCUSSION

4.1. Median SED

We generate the median SEDs of QSO1s and QSO2s (Figure 5a) to compare their ensemble properties. We begin by normalizing the best-fit SED model of each individual object at $4 \mu\text{m}$, a region with no strong polycyclic aromatic hydrocarbon emission. Next, we calculate the median and ± 25 th percentile values of the normalized SEDs at a given wavelength to obtain the normalized median SED and its dispersion. In order to compare the absolute luminosity of the two quasar types, we scale the normalized median SED according to the median of the luminosity normalizations (at $4 \mu\text{m}$) to get the final median SEDs. The quasars for which only an upper limit could be placed on the dust mass, as well as radio-loud sources, are not included when generating the median SEDs. Only the QSO1s with stellar masses are used for the median SED, but we note that the results are nearly the same if we include the objects without stellar mass measurements. The results also hold similarly if we separate each quasar type into low-redshift and high-redshift subgroups.

Relative to QSO2s, the median SED of QSO1s shows much stronger NIR and MIR emission. This is qualitatively consistent with previous works (e.g., Buchanan et al. 2006; Hiner et al. 2009; Hickox et al. 2017). The difference in the shape of the SEDs is as expected from the simple picture that the NIR and MIR emission from the hot dust surrounding the central engine is less obscured in QSO1s than in QSO2s. The FIR components of the two median SEDs overlap closely, confirming our finding that the cold dust properties of the host galaxies of the two quasar types are, on average, very similar.¹⁴ Some earlier works, by contrast, reached different conclusions (e.g., Hiner et al. 2009; Chen et al. 2015), finding that the hosts of QSO1s tend to be less FIR-luminous than those of QSO2s. This discrepancy may arise from two reasons. First, the MIR selection of the quasar samples in these previous studies may be biased in favor of intrinsically brighter QSO2s. Although Chen et al. (2015) matched their type 1 and 2 samples based

on their best-fit intrinsic AGN bolometric luminosities, it is still possible that the MIR contribution from the hosts of QSO2s is higher than that from QSO1 hosts, as the torus emission of QSO2s is intrinsically more obscured than that of QSO1s. Second, our quasars lie at lower redshifts ($z < 0.5$) than those of Chen et al. ($0.7 < z < 1.8$), and thus redshift evolution may play some role.

Figure 5b plots the ratio of the median SED of QSO1s to that of QSO2s, along side for comparison the Milky Way extinction curves of Smith et al. (2007) and Wang et al. (2015). The SED ratio rises much more steeply toward short wavelengths than either extinction curve. The SED ratio also exhibits discrete bumps at ~ 10 and $18 \mu\text{m}$ bumps, which correspond to silicate features in the extinction curve. These features in the SED ratio may not be robust in detail because the QSO2s in our sample lack spectroscopic coverage in the MIR. The clear, monotonic excess toward shorter wavelengths in the SED ratio indicates that the ISM of quasar hosts is highly optically thick in the NIR, such that the obscuration does not arise solely from galactic (Lacy et al. 2007; Hickox et al. 2017) or circumgalactic (Bowen et al. 2006; Prochaska et al. 2014; Johnson et al. 2015) scales but instead is more likely highly concentrated on nuclear scales (Ricci et al. 2017b). While the merger-driven evolutionary scenario naturally predicts that quasars should have a highly centrally concentrated distribution of ISM during their obscured (type 2) phase, we must emphasize that this expectation is at odds with the fact that the derived distributions of U_{min} for QSO1s and QSO2s are remarkably identical (Figure 3). The overall spatial distribution of the ISM, at least as crudely probed by the U_{min} parameter of the DL07 dust model, appears to be quite insensitive to the quasar type.

4.2. Implications for the Evolutionary Scenario of Quasars

Our central, underlying thesis posits that the major merger-driven, AGN feedback-mediated evolutionary picture must leave an imprint on the gas content of the constituent host galaxies. If “quasar-mode” AGN feedback is as effective as suggested by many numerical simulations (e.g., Di Matteo et al. 2005; Costa et al. 2018; however, see Debuhr et al. 2012), then the cold gas content of the host galaxy, along with its associated dust, is a key observable parameter that should reflect the evolutionary state of the system. In the absence of gas replenishment by significant external accretion during a merger episode, it stands to reason that QSO1s, as the direct by-product of dust clearing during the AGN “blow-out” phase, should have a lower cold gas content

¹⁴ We are wary that the median FIR SEDs may suffer some bias, as we exclude objects with *Herschel* non-detections. However, the bias, if any, likely may not be critical, as both quasar samples were observed in exactly the same manner by *Herschel*.

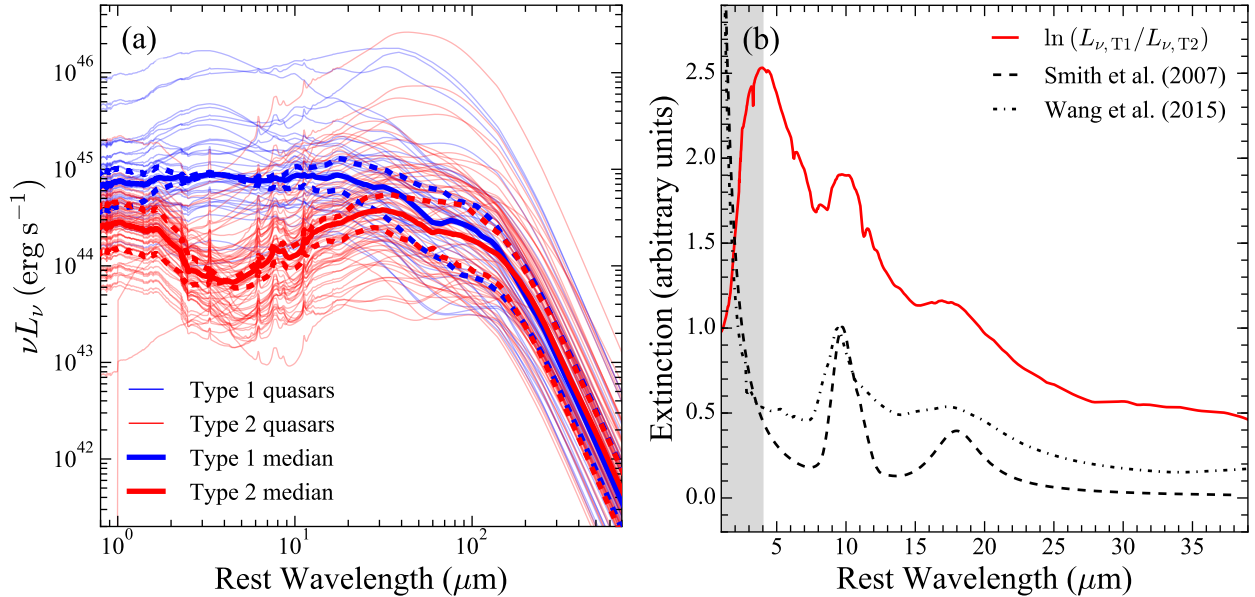


Figure 5. Comparison of median SEDs. (a) The median curves of type 1 (solid blue curve) and type 2 (solid red curve) quasars are calculated from the median of the best-fit models (thin lines) normalized at $4 \mu\text{m}$ and scaled to the median luminosities of the normalization at $4 \mu\text{m}$. The 25th–75th percentile spread of the distribution is shown as dotted lines. Type 1 quasars are significantly brighter than type 2 quasars up to $\sim 40 \mu\text{m}$. At longer wavelengths, the two types have roughly similar SEDs. (b) The ratio of the median SEDs for type 1 and type 2 quasars (red curve), which reflects the extinction if the difference between the two median SEDs is due solely to optically thin dust extinction. The ratio drops below $\sim 4 \mu\text{m}$ (shaded region) because stellar emission dominates the near-IR SED. The overall rise below $35 \mu\text{m}$ and the bumps at ~ 10 and $18 \mu\text{m}$ are features of the Milky Way extinction curve (e.g., dashed line and dot-dashed line).

than QSO2s, their immediate, highly obscured precursors. By the same token, both quasar types should also be, on average, more gas-deficient than their progenitor gas-rich galaxies.

These simple expectations are not borne out by the observations presented here. As discussed in Section 3.4, not only do obscured and unobscured quasars have comparable gas content and gas mass fraction, but both types are also essentially indistinguishable from normal, star-forming galaxies of the same stellar mass. Figure 6 further examines the dependence of the gas mass fraction on AGN bolometric luminosity. By design, the two types of quasars in our study span a similar range of AGN bolometric luminosity. We estimate the bolometric luminosity of the quasars using their [O III] luminosity as a proxy, following the formalism of Stern & Laor (2012), $\log(L_{\text{bol}}/\text{erg s}^{-1}) = 1.39 \log(L_{[\text{O III}]}/\text{erg s}^{-1}) - 13.17$. Although the bolometric luminosities have substantial uncertainties (~ 0.6 dex), as do the gas mass fractions (~ 0.3 dex), it is very surprisingly that these two parameters seem to be totally unrelated to each other. The median gas fractions of the two quasar types

are consistent with each other within the error bars.¹⁵ This was already noted by Shangguan et al. (2018) in the case of QSO1s. Here we reinforce the same conclusion for a matched sample of QSO2s.

Ho et al. (2008b,a) addressed these very issues using H I observations of type 1 AGNs. They, too, failed to find any evidence for a deficiency of gas among AGNs compared to a control sample of inactive galaxies matched in luminosity and morphological type. However, the majority of the AGNs studied by Ho et al. were quite nearby ($z \lesssim 0.1$) because of current limitations with H I observations and have luminosities too low to be deemed bona fide quasars. By contrast, the current study and that of Shangguan et al. (2018) target AGNs sufficiently powerful to constrain the canonical merger/feedback paradigm.

How to interpret these results? Taken at face value, they seem to seriously challenge the popular major merger-driven evolutionary scenario for transforming gas-rich, inactive galaxies into active systems on the one hand, and obscured (type 2) AGNs into unobscured

¹⁵ There are 7 (17), 22 (42), 18 (8), and 5 (0) QSO1s (QSO2s) used to calculate the median gas fractions with L_{bol} in $< 10^{45}$, 10^{45} – 10^{46} , 10^{46} – 10^{47} , and $> 10^{47} L_\odot$ bins, respectively.

(type 1) AGNs on the other. Perhaps galaxy mergers trigger quasar activity, but there is little direct evidence that quasar-mode feedback links the two types of quasars, or that the feedback controls the overall evolutionary cycle from normal to active and eventually to quenched galaxies. AGN-driven outflows likely recycle gas inside the galaxy instead of eject it out (e.g., Bischetti et al. 2019; Fluetsch et al. 2019). Contrary to our results, Perna et al. (2018) find that the molecular gas fraction of high-redshift ($z > 1$) obscured AGNs tends to be lower than that of main-sequence galaxies with similar mass at corresponding redshift. Quasar-mode feedback may be more effective in the high-redshift Universe when black hole accretion was more intensive.

It is unlikely that feedback only pushes the dusty ISM out of the galactic nucleus while leaving it still bound to the galaxy, as it would still be difficult to conspire to keep the interstellar radiation fields of the two quasar types so similar (Section 3.3). Nor can the problem be evaded by appealing to timing. On the one hand, although the AGN is possibly flickers on a time scale of $\sim 10^5$ Gyr (Schawinski et al. 2015), the entire episode for the black hole to intensively accrete gas (e.g., Eddington ratio $\gtrsim 0.1$) still lasts $\gtrsim 100$ Myr (Marconi et al. 2004). Fortuitously capturing the quasar just after the “blow-out” phase seems improbable. On the other hand, since quasar host galaxies have similar gas fractions as normal, star-forming galaxies, the time lag between star formation and AGN activity, if both are triggered by the same merger, should not be long. Given a gas mass of $\sim 10^{10} M_\odot$ at $M_* \approx 10^{11} M_\odot$ (Figure 4b), a moderate star formation rate of $\sim 10 M_\odot \text{ yr}^{-1}$ (Kim et al. 2006; Zakamska et al. 2016) would significantly deplete the gas content of the galaxy in merely ~ 1 Gyr.

Finally, the indistinguishable gas content would be understood trivially if the dichotomy between type 1 and type 2 quasars is merely due to viewing angle, instead of evolution. We must emphasize, however, that this explanation is not favored by various statistical differences between the two quasar types discussed in Section 1, including star formation rates (e.g., Kim et al. 2006), ionized gas velocity fields (Greene et al. 2011), radio continuum properties (Lal & Ho 2010), and local environment (Villarroel & Korn 2014). Moreover, our results hold even when the comparison between the two quasar types is restricted solely to the subset of objects triggered by galaxy mergers, whose obscuration cannot be explained purely by the traditional AGN unified model (Ricci et al. 2017a).

5. SUMMARY

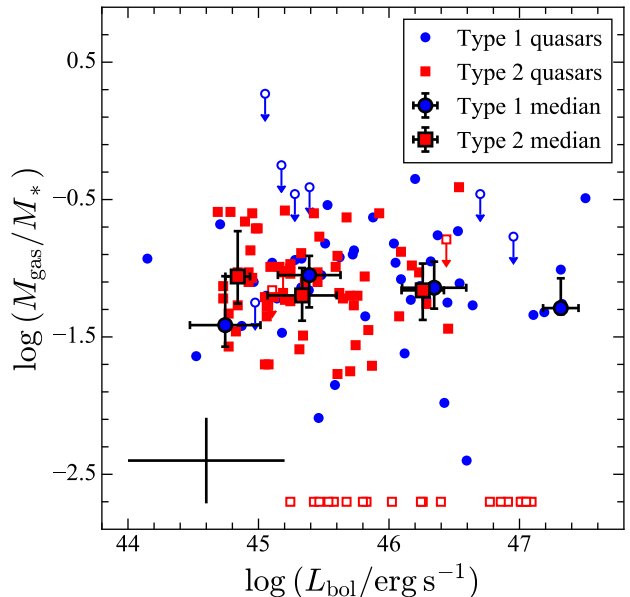


Figure 6. The gas fraction does not depend on the bolometric luminosity of the quasars. The quasars with gas mass upper limits are shown with empty symbols. The median gas fractions of the quasars of each type are calculated with L_{bol} in the ranges of $< 10^{45}$, $10^{45}\text{--}10^{46}$, $10^{46}\text{--}10^{47}$, and $> 10^{47} L_\odot$, accounting for the upper limits. The error bars represent the 25th–75th percentile ranges of the data in each bin. Type 2 quasars with upper limits in both gas and stellar masses are assigned an arbitrary mass ratio on the bottom of the plot, and they are not included in the calculation of the median gas fractions. The error bars on the lower-left corner illustrate the typical uncertainties of the bolometric luminosity and the gas fraction for the two types of quasars.

In order to test the evolutionary link between QSO1s and QSO2s, we analyze the complete IR ($\sim 1\text{--}500 \mu\text{m}$) SEDs of a sample of 86 QSO2s matched in redshift and [O III] luminosity with the sample of $z < 0.5$ Palomar-Green QSO1s recently studied in the same manner by Shangguan et al. (2018). We construct the SEDs using integrated photometric measurements based on 2MASS, WISE, and our own targeted observations acquired with the PACS and SPIRE instruments on *Herschel*. We use a newly developed fitting method with Bayesian MCMC inference to model the quasar SEDs, decomposing them into their constituent components from starlight, AGN-heated warm and hot dust from a torus, and the cold dust emission from the large-scale ISM of the host galaxy. We derive dust masses and constraints on the intensity of the interstellar radiation field. The key parameters for the cold dust component are robust with respect to the choice of models adopted for the AGN dust torus. We derive total gas masses from the

dust masses, and we estimate stellar masses from NIR photometry and optical colors.

Our main conclusions are as follows:

- The host galaxies of QSO2s, with stellar masses $M_* \approx 10^{10.3} - 10^{11.8} M_\odot$ (median $10^{10.9 \pm 0.2} M_\odot$), are as gas-rich as normal, star-forming galaxies of comparable mass, considering the 25th–75th percentiles of the sample distributions. They have total dust masses $M_d \approx 10^{6.7} - 10^{8.9} M_\odot$ (median $10^{7.7 \pm 0.3} M_\odot$), which correspond to total (atomic and molecular) gas masses of $M_{\text{gas}} \approx 10^{8.8} - 10^{11.0} M_\odot$ (median $10^{9.8 \pm 0.3} M_\odot$).
- The host galaxies of QSO2s have very similar dust/gas content and dust/gas mass fraction as the host galaxies of QSO1s. In turn, the ISM content of both types of quasars are essentially indistinguishable from that of normal, star-forming galaxies of the same stellar mass. The global gas content of quasar hosts also shows no correlation with the bolometric luminosity of the AGN.
- The interstellar radiation field of the hosts of both types of quasars is bear a close resemblance to each other, suggesting a similar spatial distribution of ISM.

- The above results are at odds with the major merger-driven evolutionary model for the transformation of QSO2s to QSO1s. Moreover, the overall similarity between the gas content of inactive galaxies and quasars poses a serious challenge to the efficacy of quasar-mode ejective feedback in galaxy evolution.
- The interstellar radiation field of quasar host galaxies is stronger than that of normal, star-forming galaxies, and it increases in intensity with increasing AGN luminosity, suggesting that the AGN heats the large-scale ISM of the host.
- The median SEDs of QSO1s and QSO2s are virtually identical in the FIR, as a consequence of their similar dust content, but differ in the MIR due to greater extinction among the obscured QSO2s.

We are grateful to an anonymous referee for helpful comments and suggestions. This work was supported by the National Science Foundation of China (11721303) and National Key R&D Program of China (2016YFA0400702). JS thanks the *Herschel* helpdesk for assistance on *Herschel* data reduction. He is grateful to Minjin Kim for useful discussions, Mingyang Zhuang for help with the dust torus models, Dongyao Zhao and Yulin Zhao for help with the stellar mass calculation and host galaxy morphology, and Yanxia Xie and Shu Wang for help with the extinction curves.

REFERENCES

- Antonucci, R. 1993, *ARA&A*, 31, 473
- Bahcall, J. N., Kirhakos, S., Saxe, D. H., & Schneider, D. P. 1997, *ApJ*, 479, 642
- Balog, Z., Müller, T., Nielbock, M., et al. 2014, *Experimental Astronomy*, 37, 129
- Bell, E. F., & de Jong, R. S. 2001, *ApJ*, 550, 212
- Bell, E. F., McIntosh, D. H., Katz, N., & Weinberg, M. D. 2003, *ApJS*, 149, 289
- Bennert, N., Canalizo, G., Jungwiert, B., et al. 2008, *ApJ*, 677, 846
- Bertram, T., Eckart, A., Fischer, S., et al. 2007, *A&A*, 470, 571
- Bessiere, P. S., Tadhunter, C. N., Ramos Almeida, C., & Villar Martín, M. 2012, *MNRAS*, 426, 276
- Bischetti, M., Maiolino, R., Carniani, S., et al. 2019, *A&A*, in press (arXiv:1806.00786)
- Blanton, M. R., & Roweis, S. 2007, *AJ*, 133, 734
- Böhm, A., Wisotzki, L., Bell, E. F., et al. 2013, *A&A*, 549, A46
- Bolatto, A. D., Wolfire, M., & Leroy, A. K. 2013, *ARA&A*, 51, 207
- Boroson, T. A., & Green, R. F. 1992, *ApJS*, 80, 109
- Boselli, A., Eales, S., Cortese, L., et al. 2010, *PASP*, 122, 261
- Bowen, D. V., Hennawi, J. F., Ménard, B., et al. 2006, *ApJL*, 645, L105
- Bruzual, G., & Charlot, S. 2003, *MNRAS*, 344, 1000
- Buchanan, C. L., Kastner, J. H., Forrest, W. J., et al. 2006, *AJ*, 132, 1890
- Chabrier, G. 2003, *PASP*, 115, 763
- Chang, Y.-Y., van der Wel, A., da Cunha, E., & Rix, H.-W. 2015, *ApJS*, 219, 8
- Chen, C.-T. J., Hickox, R. C., Alberts, S., et al. 2015, *ApJ*, 802, 50

- Cicone, C., Maiolino, R., Sturm, E., et al. 2014, *A&A*, 562, A21
- Cisternas, M., Jahnke, K., Inskip, K. J., et al. 2011, *ApJ*, 726, 57
- Ciesla, L., Boquien, M., Boselli, A., et al. 2014, *A&A*, 565, A128
- Cohen, M., Wheaton, W. A., & Megeath, S. T. 2003, *AJ*, 126, 1090
- Conroy, C. 2013, *ARA&A*, 51, 393
- Costa, T., Rosdahl, J., Sijacki, D., et al. 2018, *MNRAS*, 479, 2079
- Cutri, R. M., Wright, E. L., Conrow, T., et al. 2012, Explanatory Supplement to the WISE All-Sky Data Release Products, Tech. Rep.
- Di Matteo, T., Springel, V., & Hernquist, L. 2005, *Nature*, 433, 604
- Debuhr, J., Quataert, E., & Ma, C.-P. 2012, *MNRAS*, 420, 2221
- Draine, B. T., Dale, D. A., Bendo, G., et al. 2007, *ApJ*, 663, 866
- Draine, B. T., & Li, A. 2007, *ApJ*, 657, 810
- Dunlop, J. S., McLure, R. J., Kukuła, M. J., et al. 2003, *MNRAS*, 340, 1095
- Ellison, S. L., Patton, D. R., Mendel, J. T., & Scudder, J. M. 2011, *MNRAS*, 418, 2043
- Evans, A. S., Solomon, P. M., Tacconi, L. J., Vavilkin, T., & Downes, D. 2006, *AJ*, 132, 2398
- Fabian, A. C. 2012, *ARA&A*, 50, 455
- Feigelson, E. D., & Nelson, P. I. 1985, *ApJ*, 293, 192
- Ferrarese, L., & Merritt, D. 2000, *ApJL*, 539, L9
- Fluetsch, A., Maiolino, R., Carniani, S., et al. 2019, *MNRAS*, 483, 4586
- García-González, J., Alonso-Herrero, A., Hönig, S. F., et al. 2017, *MNRAS*, 470, 2578
- Gebhardt, K., Bender, R., Bower, G., et al. 2000, *ApJL*, 539, L13
- Genel, S., Vogelsberger, M., Springel, V., et al. 2014, *MNRAS*, 445, 175
- Greene, J. E., Zakamska, N. L., Ho, L. C., & Barth, A. J. 2011, *ApJ*, 732, 9
- Griffin, M. J., Abergel, A., Abreu, A., et al. 2010, *A&A*, 518, L3
- Grogin, N. A., Conselice, C. J., Chatzichristou, E., et al. 2005, *ApJL*, 627, L97
- Haas, M., Klaas, U., Müller, S. A. H., et al. 2003, *A&A*, 402, 87
- Harrison, C. M., Costa, T., Tadhunter, C. N., et al. 2018, *Nature Astronomy*, 2, 198
- Heckman, T. M., Smith, E. P., Baum, S. A., et al. 1986, *ApJ*, 311, 526
- Hickox, R. C., Myers, A. D., Greene, J. E., et al. 2017, *ApJ*, 849, 53
- Hiner, K. D., Canalizo, G., Lacy, M., et al. 2009, *ApJ*, 706, 508
- Ho, L. C., Darling, J., & Greene, J. E. 2008a, *ApJS*, 177, 103
- Ho, L. C., Darling, J., & Greene, J. E. 2008b, *ApJ*, 681, 128
- Hong, J., Im, M., Kim, M., & Ho, L. C. 2015, *ApJ*, 804, 34
- Hönig, S. F., & Kishimoto, M. 2010, *A&A*, 523, A27
- Hönig, S. F., & Kishimoto, M. 2017, *ApJL*, 838, L20
- Hopkins, P. F., & Hernquist, L. 2009, *ApJ*, 694, 599
- Hopkins, P. F., Hernquist, L., Cox, T. J., et al. 2006, *ApJS*, 163, 1
- Hopkins, P. F., Hernquist, L., Cox, T. J., & Kereš, D. 2008, *ApJS*, 175, 356
- Husemann, B., Davis, T. A., Jahnke, K., et al. 2017, *MNRAS*, 470, 1570
- Jarrett, T. H., Chester, T., Cutri, R., et al. 2000, *AJ*, 119, 2498
- Jarrett, T. H., Chester, T., Cutri, R., Schneider, S. E., & Huchra, J. P. 2003, *AJ*, 125, 525
- Jarrett, T. H., Cohen, M., Masci, F., et al. 2011, *ApJ*, 735, 112
- Jia, J., Ptak, A., Heckman, T., & Zakamska, N. L. 2013, *ApJ*, 777, 27
- Jogee, S. 2006, in *Lecture Notes in Physics*, Vol. 693, *Physics of Active Galactic Nuclei at all Scales*, ed. D. Alloin (Berlin: Springer), 143
- Johnson, S. D., Chen, H.-W., & Mulchaey, J. S. 2015, *MNRAS*, 452, 2553
- Kennicutt, R. C., Calzetti, D., Aniano, G., et al. 2011, *PASP*, 123, 1347
- Kewley, L. J., & Ellison, S. L. 2008, *ApJ*, 681, 1183
- Kim, M., Ho, L. C., & Im, M. 2006, *ApJ*, 642, 702
- Kim, M., Ho, L. C., Peng, C. Y., Barth, A. J., & Im, M. 2008, *ApJS*, 179, 283
- Kim, M., Ho, L. C., Peng, C. Y., Barth, A. J., & Im, M. 2017, *ApJS*, 232, 21
- Kocevski, D. D., Brightman, M., Nandra, K., et al. 2015, *ApJ*, 814, 104
- Kocevski, D. D., Faber, S. M., Mozena, M., et al. 2012, *ApJ*, 744, 148
- Kormendy, J., & Ho, L. C. 2013, *ARA&A*, 51, 511
- Kroupa, P., Tout, C. A., & Gilmore, G. 1993, *MNRAS*, 262, 545
- Lacy, M., Sajina, A., Petric, A. O., et al. 2007, *ApJL*, 669, L61
- Lagos, C. del P., Crain, R. A., Schaye, J., et al. 2015, *MNRAS*, 452, 3815
- Lal, D. V., & Ho, L. C. 2010, *AJ*, 139, 1089

- Leipski, C., Meisenheimer, K., Walter, F., et al. 2014, *ApJ*, 785, 154
- Letawe, Y., Letawe, G., & Magain, P. 2010, *MNRAS*, 403, 2088
- Lyu, J., & Rieke, G. H. 2017, *ApJ*, 841, 76
- Madau, P., & Dickinson, M. 2014, *ARA&A*, 52, 415
- Magdis, G. E., Daddi, E., Béthermin, M., et al. 2012, *ApJ*, 760, 6
- Magorrian, J., Tremaine, S., Richstone, D., et al. 1998, *AJ*, 115, 2285
- Marconi, A., Risaliti, G., Gilli, R., et al. 2004, *MNRAS*, 351, 169
- Marton, G., Calzoletti, L., Perez Garcia, A. M., et al. 2017, *arXiv:1705.05693*
- McLure, R. J., Kukula, M. J., Dunlop, J. S., et al. 1999, *MNRAS*, 308, 377
- Mechtley, M., Jahnke, K., Windhorst, R. A., et al. 2016, *ApJ*, 830, 156
- Nenkova, M., Sirocky, M. M., Ivezić, Ž., & Elitzur, M. 2008a, *ApJ*, 685, 147
- Nenkova, M., Sirocky, M. M., Nikutta, R., Ivezić, Ž., & Elitzur, M. 2008b, *ApJ*, 685, 160
- Nguyen, H. T., Schulz, B., Levenson, L., et al. 2010, *A&A*, 518, L5
- Ott, S. 2010, in *ASP Conf. Ser. 434, Astronomical Data Analysis Software and Systems XIX*, ed. Y. Mizumoto, K.-I. Morita, & M. Ohishi (San Francisco: ASP), 139
- Peng, C. Y., Ho, L. C., Impey, C. D., & Rix, H.-W. 2002, *AJ*, 124, 266
- Peng, C. Y., Ho, L. C., Impey, C. D., & Rix, H.-W. 2010, *AJ*, 139, 2097
- Pilbratt, G. L., Riedinger, J. R., Passvogel, T., et al. 2010, *A&A*, 518, L1
- Perna, M., Sargent, M. T., Brusa, M., et al. 2018, *A&A*, 619, A90
- Planck Collaboration, Ade, P. A. R., Aghanim, N., et al. 2016, *A&A*, 594, A13
- Poglitich, A., Waelkens, C., Geis, N., et al. 2010, *A&A*, 518, L2
- Prochaska, J. X., Lau, M. W., & Hennawi, J. F. 2014, *ApJ*, 796, 140
- Reyes, R., Zakamska, N. L., Strauss, M. A., et al. 2008, *AJ*, 136, 2373
- Ricci, C., Bauer, F. E., Treister, E., et al. 2017a, *MNRAS*, 468, 1273
- Ricci, C., Trakhtenbrot, B., Koss, M. J., et al. 2017b, *Nature*, 549, 488
- Saintonge, A., Catinella, B., Cortese, L., et al. 2016, *MNRAS*, 462, 1749
- Saintonge, A., Catinella, B., Tacconi, L. J., et al. 2017, *ApJS*, 233, 22
- Salpeter, E. E. 1955, *ApJ*, 121, 161
- Sanders, D. B., Soifer, B. T., Elias, J. H., et al. 1988, *ApJ*, 325, 74
- Savage, R. S., & Oliver, S. 2007, *ApJ*, 661, 1339
- Schawinski, K., Koss, M., Berney, S., & Sartori, L. F. 2015, *MNRAS*, 451, 2517
- Schmidt, M., & Green, R. F. 1983, *ApJ*, 269, 352
- Schulz, B., Marton, G., Valtchanov, I., et al. 2017, *arXiv:1706.00448*
- Scoville, N. Z., Frayer, D. T., Schinnerer, E., & Christopher, M. 2003, *ApJL*, 585, L105
- Shangguan, J., Ho, L. C., & Xie, Y. 2018, *ApJ*, 854, 158
- Shangguan, J., Ho, L. C., Li, R., et al. 2019, *ApJ*, 870, 104
- Shangguan, J., Liu, X., Ho, L. C., et al. 2016, *ApJ*, 823, 50
- Silk, J., & Rees, M. J. 1998, *A&A*, 331, L1
- Silverman, J. D., Kampczyk, P., Jahnke, K., et al. 2011, *ApJ*, 743, 2
- Skrutskie, M. F., Cutri, R. M., Stiening, R., et al. 2006, *AJ*, 131, 1163
- Smith, J. D. T., Draine, B. T., Dale, D. A., et al. 2007, *ApJ*, 656, 770
- Stern, J., & Laor, A. 2012, *MNRAS*, 426, 2703
- Tody, D. 1986, in *Proc. SPIE, Vol. 627, Instrumentation in astronomy VI*, ed. D. L. Crawford, 733
- Treister, E., Schawinski, K., Urry, C. M., & Simmons, B. D. 2012, *ApJL*, 758, L39
- Villarroel, B., & Korn, A. J. 2014, *Nature Physics*, 10, 417
- Villforth, C., Hamann, F., Rosario, D. J., et al. 2014, *MNRAS*, 439, 3342
- Villforth, C., Hamilton, T., Pawlik, M. M., et al. 2017, *MNRAS*, 466, 812
- Vito, F., Maiolino, R., Santini, P., et al. 2014, *MNRAS*, 441, 1059
- Walter, F., Carilli, C., Bertoldi, F., et al. 2004, *ApJL*, 615, L17
- Wang, R., Wagg, J., Carilli, C. L., et al. 2013, *ApJ*, 773, 44
- Wang, R., Wu, X.-B., Neri, R., et al. 2016, *ApJ*, 830, 53
- Wang, S., Li, A., & Jiang, B. W. 2015, *MNRAS*, 454, 569
- Wright, E. L., Eisenhardt, P. R. M., Mainzer, A. K., et al. 2010, *AJ*, 140, 1868
- Zakamska, N. L., Lampayan, K., Petric, A., et al. 2016, *MNRAS*, 455, 4191
- Zakamska, N. L., Strauss, M. A., Krolik, J. H., et al. 2003, *AJ*, 126, 2125
- Zhang, Z., Shi, Y., Rieke, G. H., et al. 2016, *ApJL*, 819, L27
- Zhao, D., Ho, L. C., Zhao, Y., Shangguan, J., & Kim, M. 2019, *ApJ*, submitted

Zhuang, M.-Y., Ho, L. C., & Shangguan, J. 2018, *ApJ*, 862,
118

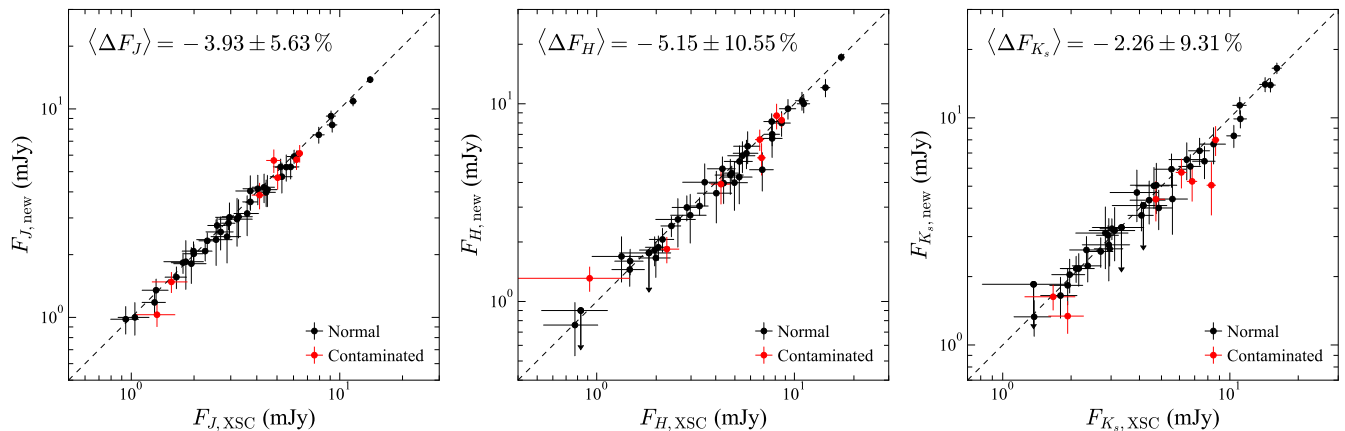


Figure 7. Comparison between our new NIR photometry with that from the 2MASS XCS, for normal (black) and contaminated (red) sources whose companions were decomposed using GALFIT. $\langle \Delta F \rangle$ is the fractional deviation in each band. Our measurements agree well with those in XCS, which tend to be slightly higher. Objects with companions or upper limits are not included in the statistics.

APPENDIX

A. COMPARISONS WITH INDEPENDENT PHOTOMETRIC MEASUREMENTS

A.1. 2MASS and WISE

We compare our aperture photometry with independent measurements listed in the 2MASS extended source catalog (XCS; Jarrett et al. 2000). There are 45 objects in our QSO2 sample that match with the XCS using a search radius of $5''$. Comparing photometry made with the same aperture radii, our measurements are reasonably consistent with those in the XCS, with the latter tending to be slightly ($\lesssim 5\%$) higher than ours (Figure 7). Our results are systematically larger if we were to compare with the default values in the catalog based on an elliptical aperture set to a K_s -band isophote of $20 \text{ mag arcsec}^{-2}$. This is expected because the default aperture size is small.

For *WISE*, we compare our measurements with those from the AllWISE catalog, which are based on PSF profile fitting. The two sets of measurements should agree well for point source targets. As shown in Figure 8, our measurements become gradually more consistent with the catalog results toward the longer wavelength bands, consistent with the fact that the targets are marginally resolved in the *W1* and *W2* bands, but increasingly pointlike in the *W3* and *W4* bands.

A.2. Herschel

In order to test the robustness of our data reduction and aperture photometry, we compare our measurements with those listed in the *Herschel*/PACS Point Source Catalog (HPPSC; Marton et al. 2017). The HPPSC measurements are based on aperture photometry on the JScanam maps from the Standard Product Generation (SPG) pipeline. The catalog provides source flux densities extracted with aperture radii $6''$ for 70 and $100 \mu\text{m}$ and $12''$ for $160 \mu\text{m}$. We compare with catalog measurements for which the S/N was determined from the “background RMS,” which closely follows our own methodology. Except for objects we identified as contaminated, 73, 77, and 59 objects in our QSO2 sample have measurements at 70, 100, and $160 \mu\text{m}$ listed in IRSA.

Figure 9 shows that the consistency is very good at 70 and $100 \mu\text{m}$. The systematic deviations, $\lesssim 1\%$, are much smaller than the scatter ($\sim 10\%$). However, at $160 \mu\text{m}$ the systematic deviation is comparable to the $\sim 10\%$ scatter. This is due, on the one hand, to the different aperture sizes we adopt, and, on the other hand, to the different algorithms used to generate the maps. If we choose the same aperture set as HPPSC, the systematic deviation drops to 6.5%, which can be explained fully by the differences of the maps generated by JScanam and HPF methods¹⁶. The median

¹⁶ We tested the aperture photometry performed based on three different algorithms (HPF, JScanam, and Unimap) for generating `1eve12.5` maps from the SPG14 pipeline. We find that the HPF method produces maps with the smallest uncertainty, although different settings (e.g., the HPF radius) can change the noise level of the HPF maps. Maps created using the JScanam and Unimap algorithms show no systematic deviations relative to HPF at 70 and $100 \mu\text{m}$, but their flux densities are systematically lower by 6.7% and 9.1% at $160 \mu\text{m}$

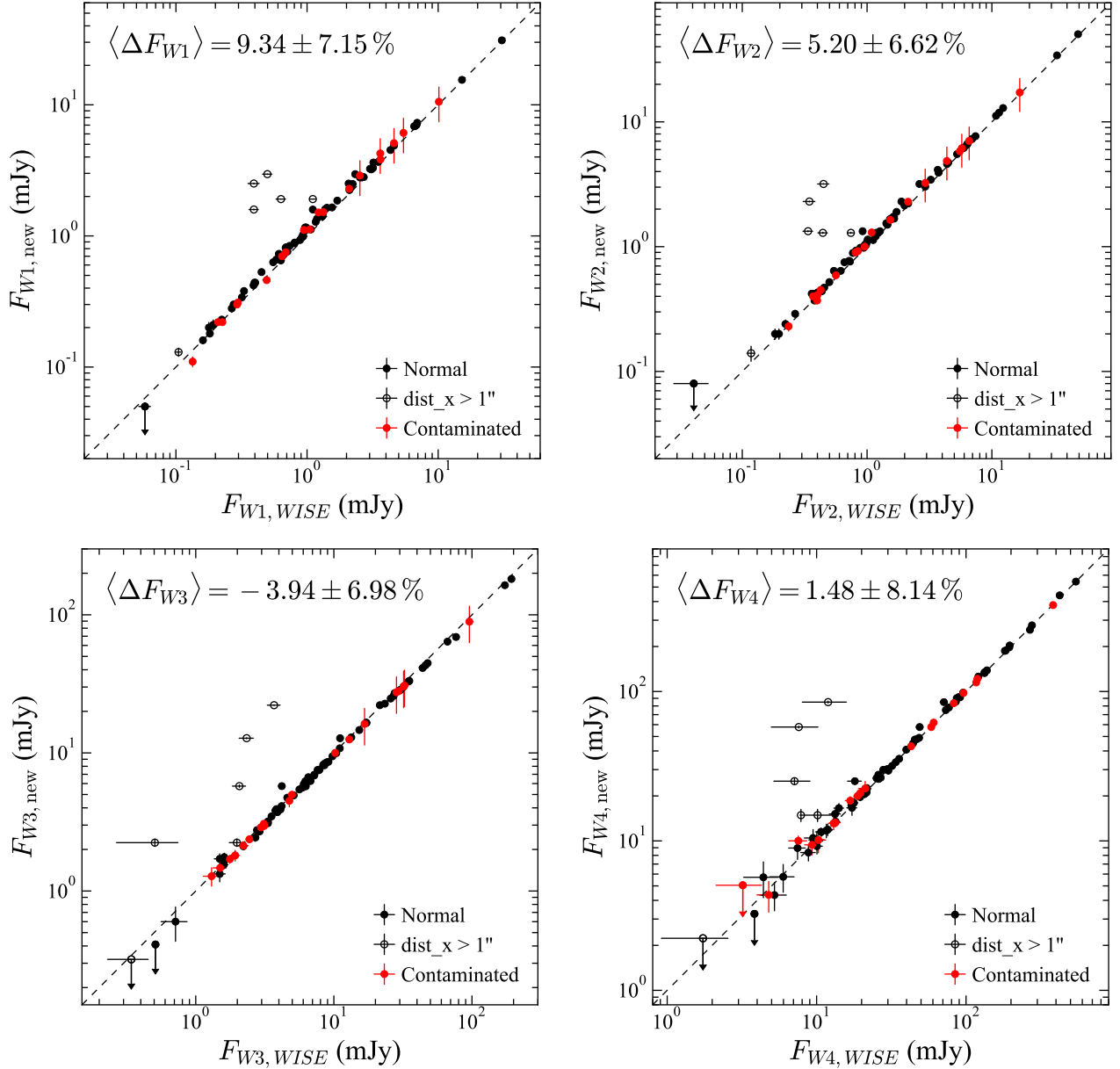


Figure 8. Comparison between our new MIR photometry with that from the AllWISE catalog, for normal sources (filled black symbols), contaminated sources with companions removed using GALFIT (red symbols), and objects with positions in the catalog deviating $> 1''$ from our nominal positions (open black symbols). All sources with atypically large flux deviations are open symbols; they are likely mismatched. $\langle \Delta F \rangle$ is the fractional deviation in each band. Our measurements tend to be systematically higher ($\sim 10\%$) than the catalog values in W1, marginally higher (5%) in W2, and consistent in W3 and W4. Only the normal, detected objects are included in the statistics.

uncertainties of the HPPSC measurements are 5.55, 5.39, and 11.92 mJy at 70, 100, and 160 μm , respectively, while the corresponding values for our measurements are 3.36, 3.99, and 12.15 mJy. The differences can also be explained by the different aperture sizes and the different algorithms used to generate the maps. Our measured uncertainties are also comparable to those reported for the PG sample of QSO1s (Shangguan et al. 2018).

μm . Therefore, we adopt the HPF method to generate the maps ourselves, in order to reduce the noise, but we restrict to the parameters provided by Balog et al. (2014).

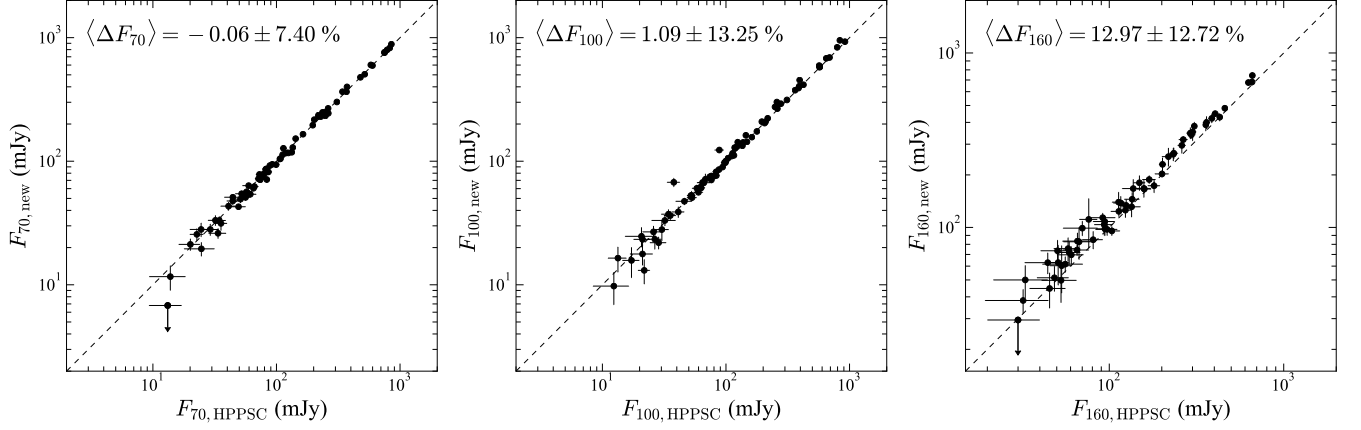


Figure 9. Comparison between our new PACS flux densities and those from HPPSC in the 70, 100, and 160 μm bands. Objects with flux densities lower than 3 times of the background RMS are replaced with 3σ as upper limits. The median fractional deviation and its standard deviation, $\langle\Delta F\rangle$, are shown in the upper-left corner of each plot. The scatter in all three bands is $\sim 10\%$. For 70 and 100 μm , the systematic deviation is negligible. The $\sim 10\%$ systematic deviation at 160 μm is significant; it can be explained by the usage of different aperture radii and algorithms to generate maps (see main text).

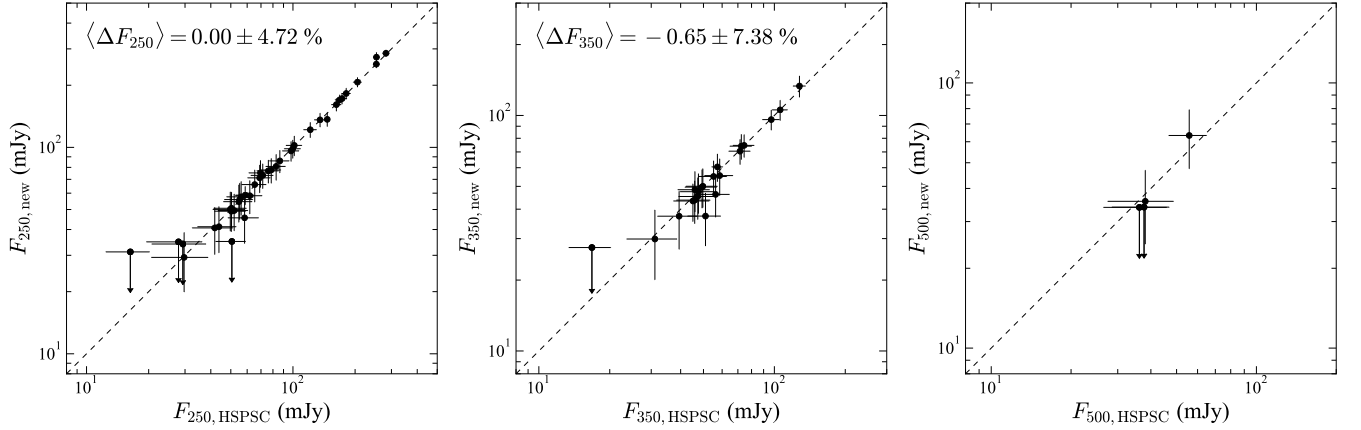


Figure 10. Comparison between our new SPIRE flux densities and those from HPPSC in the 250, 350, and 500 μm bands. Objects with flux densities lower than 3 times of the background RMS are replaced with 3σ as upper limits. The median fractional deviation and its standard deviation, $\langle\Delta F\rangle$, are shown in the upper-left corner of each plot. Only a few objects are undetected; these are not included in the statistics. For 250 and 350 μm , the scatter is $\lesssim 10\%$, compared to which the systematic deviations are negligible. The number of objects at 500 μm is not enough to draw firm conclusions, although the consistency for the four objects is still good.

As for SPIRE, 39, 21, and 4 objects at 250, 350, and 500 μm match the HSPSC within a search radius of $20''$ from the optical positions of the QSO2s. Our measurements in the first two bands are very well consistent with those in HSPSC (Figure 10). For the 500 μm band, there are not enough objects to draw firm conclusions, but the consistency is still encouraging.

B. THE INFLUENCE OF DIFFERENT DUST TORUS MODELS

We evaluate the impact of the choice of dust torus model (CLUMPY vs. CAT3D) on the derived dust mass, U_{min} , and IR luminosity. The CLUMPY template used in the fits is the median torus template derived by Shangguan et al. (2018) based on their SED decomposition of the PG quasars. We make this simplifying assumption in order to reduce the number of free parameters in the fitting. In general, the CLUMPY template provides more emission in the $W3$ band but less emission in the $W4$ band compared to the data. As in Shangguan et al. (2018), we add a blackbody component to account for the possible presence of hot dust emission, which is often needed for QSO1s, but we find

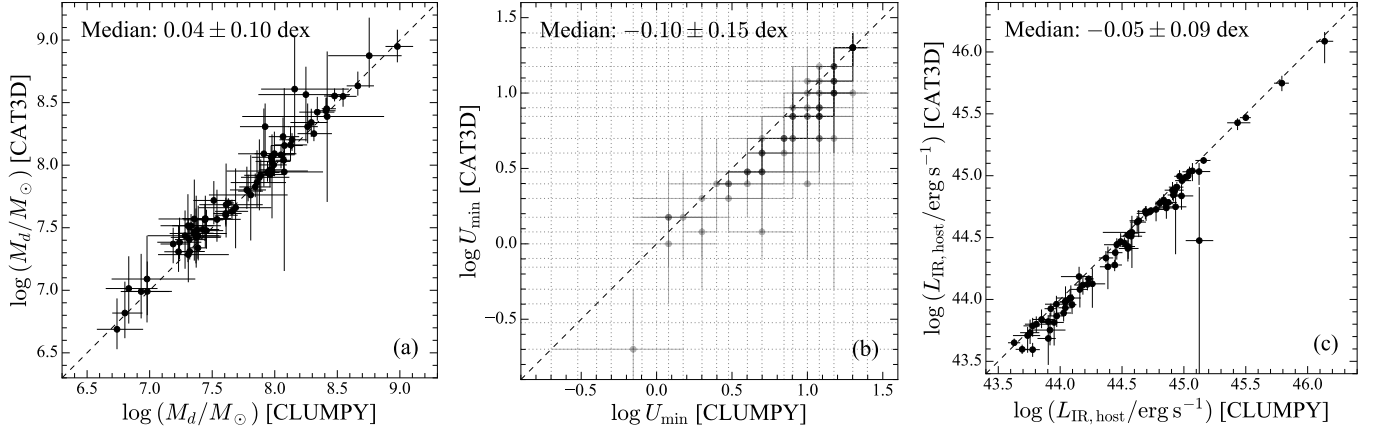


Figure 11. SED fits that adopt CAT3D or CLUMPY torus models produce consistent values of (a) dust mass, (b) U_{\min} , and (c) IR luminosity of the host galaxy. The discreteness of U_{\min} produces some overlapping data points on the grids; the darker symbols reflect grids with more data.

that it is usually negligible for QSO2s. The CAT3D models of both [Hönig & Kishimoto \(2017\)](#) and [García-González et al. \(2017\)](#) generally produce results consistent with those based on CLUMPY. In detail, the templates of Hönig & Kishimoto tend to fit the overall SED better, while the templates of García-González et al. produce fitted parameters that show closer agreement with those based on CLUMPY. Figure 11 directly compares the fitting results for the templates of CLUMPY and Hönig & Kishimoto. The dust masses derived using CAT3D tend to be slightly higher than those using CLUMPY, while U_{\min} and $L_{\text{IR,host}}$ are slightly lower. This is consistent with the fact that the CLUMPY template drops quickly toward the FIR, while the best-fit templates from CAT3D are more extended. In any event, the systematic differences are quite small, and we conclude that the key quantities in our work (M_d , U_{\min} , and $L_{\text{IR,host}}$) are not sensitive to the choice of the dust torus model.

Table 1. Physical Properties of Type 2 Quasars

Object	R.A.	Dec.	z	$\log L_{[\text{O III}]}$	$\log U_{\text{min}}$	$\log M_d$	$\log M_*$	$\log \delta_{\text{GDR}}$	$\log M_{\text{gas}}$
	(J2000)	(J2000)		(L_{\odot})		(M_{\odot})	(M_{\odot})		(M_{\odot})
(1)	(2)	(3)	(4)	(5)	(6)	(7)	(8)	(9)	(10)
SDSS J0041-0952	00 41 13.75	-09 52 31.7	0.095	8.31	$0.40^{+0.20}_{-0.22}$	$7.53^{+0.18}_{-0.21}$	10.89 ± 0.22	2.09	9.61 ± 0.28
SDSS J0119-1026	01 19 35.64	-10 26 13.1	0.125	8.40	$0.70^{+0.30}_{-0.22}$	$7.57^{+0.19}_{-0.24}$	10.67 ± 0.22	2.09	9.65 ± 0.30
SDSS J0202+1247	02 02 23.71	+12 47 17.7	0.086	8.11	$0.48^{+0.22}_{-0.08}$	$8.09^{+0.09}_{-0.12}$	10.77 ± 0.24	2.09	10.18 ± 0.22
SDSS J0339-0548	03 39 23.15	-05 48 41.6	0.085	8.22	$0.84^{+0.06}_{-0.15}$	$7.34^{+0.14}_{-0.06}$	10.30 ± 0.22	2.09	9.43 ± 0.22
SDSS J0747+3200	07 47 51.57	+32 00 52.1	0.280	8.93	$0.84^{+0.06}_{-0.15}$	$8.43^{+0.14}_{-0.08}$	11.12 ± 0.25	2.09	10.52 ± 0.23
SDSS J0752+2510	07 52 26.52	+25 10 20.2	0.239	8.69	$1.00^{+0.18}_{-0.30}$	$8.07^{+0.19}_{-0.17}$	11.15 ± 0.25	2.09	10.16 ± 0.27
SDSS J0753+3847	07 53 24.38	+38 47 31.8	0.097	8.21	$0.70^{+0.15}_{-0.10}$	$7.81^{+0.11}_{-0.13}$	10.93 ± 0.23	2.09	9.90 ± 0.23
SDSS J0753+2309	07 53 29.94	+23 09 30.7	0.337	8.57	...	< 8.70	< 11.23	2.08	< 10.78
SDSS J0759+5050	07 59 40.96	+50 50 24.1	0.054	8.77	$1.30^{+0.10}_{-0.22}$	$7.32^{+0.10}_{-0.07}$	10.61 ± 0.21	2.09	9.41 ± 0.22
SDSS J0802+2552	08 02 52.93	+25 52 55.6	0.081	8.77	$1.30^{+0.10}_{-0.22}$	$7.34^{+0.09}_{-0.08}$	11.18 ± 0.21	2.09	9.43 ± 0.22
SDSS J0802+3046	08 02 18.65	+30 46 22.7	0.077	8.14	$0.90^{+0.27}_{-0.20}$	$7.03^{+0.23}_{-0.20}$	10.58 ± 0.23	2.09	9.12 ± 0.30
SDSS J0803+3926	08 03 37.32	+39 26 33.1	0.066	8.10	$0.70^{+0.20}_{-0.22}$	$7.38^{+0.14}_{-0.13}$	11.03 ± 0.21	2.09	9.46 ± 0.24
SDSS J0805+2818	08 05 23.30	+28 18 15.8	0.128	8.59	$0.90^{+0.10}_{-0.06}$	$8.20^{+0.06}_{-0.08}$	11.31 ± 0.22	2.09	10.28 ± 0.21
SDSS J0811+4442	08 11 00.20	+44 42 16.4	0.183	8.25	$0.48^{+0.00}_{-0.08}$	$8.56^{+0.06}_{-0.04}$	11.36 ± 0.23	2.09	10.65 ± 0.21
SDSS J0818+3604	08 18 42.36	+36 04 09.7	0.076	8.49	$1.08^{+0.22}_{-0.38}$	$6.71^{+0.27}_{-0.17}$	10.39 ± 0.22	2.09	8.80 ± 0.30
SDSS J0823+3132	08 23 13.50	+31 32 03.8	0.433	9.72	...	< 8.80	< 11.66	2.13	< 10.93
SDSS J0825+2025	08 25 27.51	+20 25 43.5	0.336	8.86	...	< 8.60	< 11.39	2.09	< 10.69
SDSS J0835+5240	08 35 23.83	+52 40 55.0	0.117	8.38	$0.90^{+0.18}_{-0.20}$	$8.14^{+0.13}_{-0.12}$	11.21 ± 0.22	2.09	10.22 ± 0.24
SDSS J0840+3320	08 40 28.60	+33 20 52.3	0.167	8.50	$0.18^{+0.22}_{-0.18}$	$8.27^{+0.16}_{-0.19}$	11.25 ± 0.24	2.09	10.36 ± 0.27
SDSS J0841+0334	08 41 07.07	+03 34 41.3	0.274	8.75	...	< 8.00	< 11.22	2.08	< 10.08
SDSS J0843+3549	08 43 44.99	+35 49 42.0	0.054	8.10	$0.60^{+0.10}_{-0.12}$	$7.50^{+0.09}_{-0.07}$	10.92 ± 0.21	2.09	9.59 ± 0.21
SDSS J0843+2944	08 43 09.87	+29 44 04.9	0.398	9.30	...	< 8.60	11.49 ± 0.25	2.10	< 10.70
SDSS J0848+0136	08 48 56.58	+01 36 47.8	0.350	8.44	...	< 8.60	< 11.67	2.13	< 10.73
SDSS J0850+3039	08 50 38.15	+30 39 32.3	0.179	8.60	...	< 8.10	< 10.68	2.11	< 10.21
SDSS J0858+3121	08 58 10.64	+31 21 36.3	0.139	8.50	$1.08^{+0.22}_{-0.38}$	$7.27^{+0.29}_{-0.21}$	10.54 ± 0.23	2.09	9.36 ± 0.32
SDSS J0907+5211	09 07 54.09	+52 11 27.5	0.085	8.21	$0.60^{+0.10}_{-0.00}$	$7.50^{+0.04}_{-0.09}$	10.69 ± 0.23	2.09	9.59 ± 0.21
SDSS J0918+2357	09 18 19.66	+23 57 36.5	0.419	9.54	...	< 8.70	< 11.54	2.11	< 10.81
SDSS J0926+0724	09 26 35.12	+07 24 46.5	0.190	8.41	$0.48^{+0.00}_{-0.08}$	$8.41^{+0.08}_{-0.04}$	11.08 ± 0.23	2.09	10.50 ± 0.21
SDSS J0936+5924	09 36 25.37	+59 24 52.7	0.096	8.34	...	< 7.30	10.58 ± 0.21	2.12	< 9.42
SDSS J1002+0551	10 02 02.08	+05 51 45.6	0.208	8.87	$0.84^{+0.33}_{-0.37}$	$7.71^{+0.35}_{-0.27}$	11.25 ± 0.23	2.09	9.80 ± 0.37
SDSS J1022+4734	10 22 57.00	+47 34 54.4	0.144	8.31	$0.40^{+0.30}_{-0.32}$	$7.69^{+0.31}_{-0.31}$	11.12 ± 0.21	2.09	9.77 ± 0.37
SDSS J1032+4926	10 32 52.60	+49 26 12.9	0.119	8.30	$0.84^{+0.33}_{-0.45}$	$7.09^{+0.37}_{-0.33}$	10.88 ± 0.24	2.09	9.18 ± 0.40
SDSS J1034+6001	10 34 08.59	+60 01 52.1	0.051	8.81	$0.90^{+0.10}_{-0.06}$	$7.69^{+0.05}_{-0.06}$	10.97 ± 0.20	2.09	9.77 ± 0.21
SDSS J1040+4745	10 40 14.43	+47 45 54.7	0.486	9.77	$1.30^{+0.10}_{-0.22}$	$8.92^{+0.16}_{-0.11}$	< 11.79	2.09	11.01 ± 0.24
SDSS J1044+3008	10 44 02.40	+30 08 34.0	0.497	9.64	$0.40^{+0.51}_{-0.40}$	$8.57^{+0.46}_{-0.51}$	< 11.80	2.09	10.65 ± 0.52
SDSS J1052+0609	10 52 08.20	+06 09 15.2	0.052	8.15	$0.70^{+0.00}_{-0.10}$	$7.46^{+0.07}_{-0.06}$	10.57 ± 0.21	2.09	9.54 ± 0.21
SDSS J1100+0846	11 00 12.39	+08 46 16.4	0.100	9.11	$1.08^{+0.10}_{-0.08}$	$7.98^{+0.07}_{-0.08}$	11.05 ± 0.22	2.09	10.07 ± 0.21
SDSS J1100+4951	11 00 33.49	+49 51 19.7	0.135	8.07	$0.08^{+0.40}_{-0.23}$	$7.80^{+0.30}_{-0.36}$	11.11 ± 0.21	2.09	9.89 ± 0.39
SDSS J1101+4004	11 01 40.57	+40 04 22.8	0.457	9.71	...	< 8.90	< 11.68	2.13	< 11.03
SDSS J1102+6459	11 02 13.02	+64 59 24.8	0.078	8.44	$1.30^{+0.10}_{-0.12}$	$7.60^{+0.08}_{-0.07}$	10.92 ± 0.21	2.09	9.68 ± 0.21
SDSS J1109+2659	11 09 38.00	+26 59 59.1	0.328	8.75	$1.08^{+0.10}_{-0.08}$	$8.55^{+0.08}_{-0.07}$	11.27 ± 0.25	2.09	10.64 ± 0.21
SDSS J1109+4233	11 09 52.83	+42 33 15.7	0.261	9.37	$1.30^{+0.10}_{-0.12}$	$8.63^{+0.11}_{-0.07}$	11.13 ± 0.25	2.09	10.72 ± 0.22
SDSS J1110+5848	11 10 15.25	+58 48 45.9	0.143	8.84	$-0.70^{+0.40}_{-0.30}$	$8.58^{+0.19}_{-0.32}$	< 10.46	2.09	10.66 ± 0.33
SDSS J1111-0053	11 11 00.61	-00 53 34.8	0.090	8.07	$1.30^{+0.10}_{-0.12}$	$7.93^{+0.10}_{-0.06}$	11.14 ± 0.21	2.09	10.01 ± 0.21

Table 1 continued

Table 1 (continued)

Object	R.A.	Dec.	z	$\log L_{[\text{O III}]}$	$\log U_{\text{min}}$	$\log M_d$	$\log M_*$	$\log \delta_{\text{GDR}}$	$\log M_{\text{gas}}$
	(J2000)	(J2000)		(L_{\odot})		(M_{\odot})	(M_{\odot})		(M_{\odot})
(1)	(2)	(3)	(4)	(5)	(6)	(7)	(8)	(9)	(10)
SDSS J1123+3105	11 23 30.93	+31 05 19.3	0.310	9.15	$0.84^{+0.16}_{-0.15}$	$8.30^{+0.17}_{-0.13}$	11.42 ± 0.23	2.09	10.39 ± 0.25
SDSS J1137+5731	11 37 10.78	+57 31 58.8	0.395	9.60	...	< 8.80	< 11.48	2.10	< 10.90
SDSS J1145+0241	11 45 44.99	+02 41 26.9	0.128	8.19	$0.08^{+0.10}_{-0.08}$	$8.21^{+0.11}_{-0.11}$	10.96 ± 0.21	2.09	10.30 ± 0.23
SDSS J1151+0049	11 51 38.25	+00 49 46.4	0.195	8.40	...	< 7.80	10.92 ± 0.25	2.09	< 9.89
SDSS J1152+1016	11 52 45.66	+10 16 23.8	0.070	8.70	$1.00^{+0.30}_{-0.40}$	$6.82^{+0.25}_{-0.21}$	10.67 ± 0.21	2.09	8.90 ± 0.30
SDSS J1153+5806	11 53 26.43	+58 06 44.6	0.065	8.44	$0.84^{+0.16}_{-0.15}$	$7.41^{+0.12}_{-0.10}$	10.50 ± 0.21	2.09	9.50 ± 0.23
SDSS J1200+3147	12 00 41.41	+31 47 45.9	0.116	9.31	$0.84^{+0.33}_{-0.45}$	$7.47^{+0.28}_{-0.25}$	11.00 ± 0.22	2.09	9.56 ± 0.33
SDSS J1218+0222	12 18 35.45	+02 22 39.9	0.213	8.85	$1.18^{+0.12}_{-0.18}$	$8.00^{+0.11}_{-0.10}$	11.15 ± 0.23	2.09	10.09 ± 0.23
SDSS J1230+3943	12 30 06.79	+39 43 19.3	0.407	9.74	$0.40^{+0.51}_{-0.49}$	$8.34^{+0.50}_{-0.52}$	< 11.56	2.09	10.42 ± 0.55
SDSS J1238+0927	12 38 43.45	+09 27 36.6	0.083	8.51	$0.70^{+0.20}_{-0.30}$	$7.45^{+0.19}_{-0.18}$	11.03 ± 0.21	2.09	9.54 ± 0.27
SDSS J1238+6703	12 38 04.82	+67 03 20.8	0.180	8.23	$0.48^{+0.00}_{-0.08}$	$8.40^{+0.08}_{-0.08}$	11.09 ± 0.23	2.09	10.49 ± 0.22
SDSS J1240+3534	12 40 37.84	+35 34 37.3	0.161	8.70	$1.18^{+0.12}_{-0.10}$	$7.98^{+0.15}_{-0.10}$	10.98 ± 0.22	2.09	10.07 ± 0.24
SDSS J1258+5239	12 58 50.78	+52 39 13.1	0.055	8.23	$0.18^{+0.12}_{-0.10}$	$7.62^{+0.10}_{-0.11}$	10.78 ± 0.21	2.09	9.71 ± 0.23
SDSS J1300+5454	13 00 38.10	+54 54 36.9	0.088	8.89	$0.90^{+0.27}_{-0.43}$	$7.02^{+0.32}_{-0.21}$	10.82 ± 0.22	2.09	9.11 ± 0.33
SDSS J1316+4452	13 16 39.74	+44 52 35.1	0.091	8.57	$1.18^{+0.00}_{-0.18}$	$8.04^{+0.07}_{-0.06}$	10.72 ± 0.24	2.09	10.12 ± 0.21
SDSS J1323+6104	13 23 45.99	+61 04 00.2	0.071	8.15	$0.40^{+0.08}_{-0.22}$	$7.38^{+0.13}_{-0.12}$	10.73 ± 0.21	2.09	9.46 ± 0.24
SDSS J1323-0159	13 23 23.34	-01 59 41.9	0.350	9.27	$0.84^{+0.23}_{-0.37}$	$8.10^{+0.27}_{-0.30}$	< 11.40	2.09	10.19 ± 0.35
SDSS J1332+4632	13 32 22.45	+46 32 26.6	0.363	9.17	...	< 8.60	< 11.49	2.10	< 10.70
SDSS J1335+6316	13 35 42.50	+63 16 41.5	0.169	8.44	$1.30^{+0.10}_{-0.12}$	$7.78^{+0.12}_{-0.09}$	10.90 ± 0.23	2.09	9.86 ± 0.23
SDSS J1348+5130	13 48 18.11	+51 30 22.4	0.333	8.68	$-0.10^{+0.27}_{-0.43}$	$8.94^{+0.31}_{-0.34}$	< 11.36	2.09	11.02 ± 0.38
SDSS J1356+0132	13 56 21.86	+01 32 23.7	0.173	8.33	$1.00^{+0.18}_{-0.16}$	$7.93^{+0.12}_{-0.14}$	11.01 ± 0.23	2.09	10.02 ± 0.24
SDSS J1356+4304	13 56 37.05	+43 04 03.8	0.193	9.00	...	< 8.00	< 10.75	2.10	< 10.10
SDSS J1356+1026	13 56 46.11	+10 26 09.1	0.123	9.19	$1.30^{+0.10}_{-0.12}$	$7.92^{+0.13}_{-0.09}$	11.27 ± 0.22	2.09	10.01 ± 0.23
SDSS J1356+4259	13 56 54.26	+42 59 16.9	0.195	8.30	$1.08^{+0.22}_{-0.23}$	$7.78^{+0.19}_{-0.16}$	11.08 ± 0.23	2.09	9.87 ± 0.27
SDSS J1358+4741	13 58 22.78	+47 41 02.7	0.131	8.35	$0.90^{+0.18}_{-0.06}$	$8.01^{+0.06}_{-0.11}$	11.30 ± 0.21	2.09	10.09 ± 0.22
SDSS J1405+4026	14 05 41.21	+40 26 32.5	0.081	8.71	$1.00^{+0.30}_{-0.30}$	$7.29^{+0.19}_{-0.16}$	10.56 ± 0.21	2.09	9.38 ± 0.26
SDSS J1407+5851	14 07 12.95	+58 51 20.5	0.171	8.26	$0.48^{+0.12}_{-0.08}$	$8.16^{+0.10}_{-0.13}$	10.96 ± 0.23	2.09	10.25 ± 0.23
SDSS J1413-0142	14 13 15.30	-01 42 21.0	0.380	9.16	$1.40^{+0.00}_{-0.10}$	$8.24^{+0.08}_{-0.05}$	< 11.58	2.09	10.32 ± 0.21
SDSS J1430+1339	14 30 29.89	+13 39 12.1	0.085	9.04	$1.18^{+0.12}_{-0.18}$	$7.62^{+0.12}_{-0.10}$	11.06 ± 0.21	2.09	9.71 ± 0.23
SDSS J1437+3011	14 37 37.85	+30 11 01.1	0.092	8.80	$1.08^{+0.10}_{-0.23}$	$7.49^{+0.15}_{-0.13}$	11.14 ± 0.21	2.09	9.58 ± 0.24
SDSS J1450-0106	14 50 19.19	-01 06 47.5	0.119	8.41	$0.40^{+0.30}_{-0.32}$	$7.61^{+0.28}_{-0.32}$	10.93 ± 0.21	2.09	9.70 ± 0.36
SDSS J1455+3226	14 55 19.41	+32 26 01.8	0.087	8.60	$0.30^{+0.18}_{-0.22}$	$7.72^{+0.15}_{-0.18}$	10.58 ± 0.22	2.09	9.81 ± 0.26
SDSS J1513+4319	15 13 15.07	+43 19 59.7	0.208	9.05	$0.60^{+0.10}_{-0.12}$	$8.33^{+0.13}_{-0.12}$	11.30 ± 0.22	2.09	10.42 ± 0.24
SDSS J1552+2753	15 52 25.67	+27 53 43.5	0.074	8.40	$0.40^{+0.20}_{-0.10}$	$7.58^{+0.14}_{-0.17}$	10.85 ± 0.21	2.09	9.67 ± 0.25
SDSS J1558+3513	15 58 29.37	+35 13 28.7	0.119	8.73	$0.60^{+0.40}_{-0.30}$	$7.51^{+0.28}_{-0.30}$	10.82 ± 0.21	2.09	9.60 ± 0.35
SDSS J1605+0742	16 05 58.01	+07 42 04.3	0.337	8.65	$1.18^{+0.12}_{-0.48}$	$7.81^{+0.26}_{-0.20}$	< 11.44	2.09	9.89 ± 0.30
SDSS J1616+4321	16 16 54.99	+43 21 30.5	0.186	8.79	$1.08^{+0.22}_{-0.23}$	$7.57^{+0.23}_{-0.17}$	10.93 ± 0.23	2.09	9.66 ± 0.28
SDSS J1624+3344	16 24 36.41	+33 44 06.8	0.122	8.52	$0.84^{+0.23}_{-0.45}$	$7.45^{+0.27}_{-0.28}$	10.64 ± 0.21	2.09	9.54 ± 0.34
SDSS J1641+4321	16 41 26.91	+43 21 21.6	0.221	8.59	$1.00^{+0.18}_{-0.30}$	$7.83^{+0.21}_{-0.21}$	11.01 ± 0.25	2.09	9.91 ± 0.29
SDSS J2133+1009	21 33 40.83	+10 09 29.2	0.126	8.44	$0.60^{+0.10}_{-0.00}$	$8.06^{+0.07}_{-0.08}$	11.12 ± 0.21	2.09	10.15 ± 0.21
SDSS J2134-0749	21 34 00.61	-07 49 42.7	0.089	8.32	$1.18^{+0.12}_{-0.27}$	$6.74^{+0.21}_{-0.16}$	10.53 ± 0.22	2.09	8.83 ± 0.27
SDSS J2144-0810	21 44 25.53	-08 10 29.4	0.158	8.04	$0.08^{+0.32}_{-0.23}$	$8.01^{+0.26}_{-0.33}$	10.69 ± 0.24	2.09	10.10 ± 0.35

NOTE— (1) Source name. (2) and (3) J2000 coordinates. (4) Redshift. (5) [O III] λ 5007 luminosity from [Reyes et al. \(2008\)](#). (6) Best-fit minimum intensity of the interstellar radiation field relative to that measured in the solar neighborhood. The quoted uncertainties represent the 68 percent confidence interval determined from the 16th and 84th percentile of the marginalized posterior probability density function. However, if there are fewer than 16% sampled values at the discrete grids below (above) the best-fit value, the lower (upper) uncertainty of the parameter is not resolved, and it is reported as “0.00” in the table. (7) Best-fit total dust mass. (8) Stellar mass derived from optical color and J -band absolute magnitude ([Bell & de Jong 2001](#)), converted to [Chabrier \(2003\)](#) IMF. (9) Gas-to-dust ratio estimated in Section 3.4. (10) Total gas mass including helium and heavier elements.

Table 2. NIR and MIR Photometry

Object	$r_{2\text{MASS}}$	F_J	F_H	F_{K_s}	F_{W1}	F_{W2}	F_{W3}	F_{W4}
	($''$)	(mJy)	(mJy)	(mJy)	(mJy)	(mJy)	(mJy)	(mJy)
(1)	(2)	(3)	(4)	(5)	(6)	(7)	(8)	(9)
SDSS J0041-0952	20	3.02±0.53	3.97±0.85	5.94±1.01	1.91±0.01	1.29±0.02	2.24±0.15	14.87±1.46
SDSS J0119-1026	7	1.00±0.18	1.45±0.26	1.65±0.34	1.02±0.01	1.08±0.03	4.93±0.14	20.61±1.23
SDSS J0202+1247	20	2.96±0.77	4.26±1.15	<4.11	4.52±0.02	6.20±0.02	22.73±0.13	75.14±1.06
SDSS J0339-0548	10	1.00±0.19	1.17±0.28	1.51±0.42	0.93±0.01	0.98±0.02	6.23±0.15	21.08±1.16
SDSS J0747+3200	7	0.42±0.13	0.90±0.19	0.86±0.26	0.42±0.02	0.44±0.02	3.47±0.16	17.97±1.47
SDSS J0752+2510	7	0.69±0.19	<0.86	<0.89	0.97±0.02	1.68±0.03	8.14±0.18	29.53±1.65
SDSS J0753+3847	20	3.15±0.69	3.53±1.04	<3.29	1.51±0.02	1.30±0.03	4.98±0.13 ^a	20.91±1.71
SDSS J0753+2309	7	<0.33	<0.59	<0.65	0.21±0.02	0.24±0.02	1.33±0.17	10.16±1.38
SDSS J0759+5050	20	5.27±0.67	4.64±1.03	6.44±1.06	3.67±0.02	7.29±0.02	63.93±0.14	277.22±1.21
SDSS J0802+2552	20	8.38±0.66	9.44±1.10	9.89±0.89	7.29±0.02	12.91±0.03	69.09±0.17	258.77±1.79
SDSS J0802+3046	20	2.36±0.59	4.69±0.71	3.11±0.95	2.81±0.02	3.03±0.03	6.26±0.17	26.30±1.43
SDSS J0803+3926	20	9.24±0.56	10.00±1.03	11.35±0.99	5.10±1.53	6.15±1.85	30.75±9.22	114.97±1.41
SDSS J0805+2818	20	4.10±0.71	6.10±1.14	5.02±1.04	2.51±0.03	2.30±0.03	12.78±0.17	57.83±1.12
SDSS J0811+4442	20	2.08±0.42	2.99±0.61	2.63±0.85	1.13±0.02	1.03±0.02	6.24±0.14	21.77±1.34
SDSS J0818+3604	10	1.58±0.26	1.89±0.42	1.56±0.39	1.65±0.03	3.93±0.03	28.56±0.17	91.50±1.68
SDSS J0823+3132	7	<0.45	<0.67	<0.74	0.16±0.01	0.37±0.02	2.70±0.16	10.46±1.51
SDSS J0825+2025	7	<0.48	<0.77	<0.62	<0.05	<0.08	0.60±0.17	5.71±1.56
SDSS J0835+5240	20	4.04±0.75	5.11±1.03	4.39±1.33	2.79±0.01	3.98±0.02	16.50±0.13	91.85±1.05
SDSS J0840+3320	15	1.97±0.48	<2.21	2.39±0.63	1.16±0.02	1.29±0.03	6.86±0.17	26.51±1.68
SDSS J0841+0334	7	<0.56	<0.85	<1.09	0.44±0.02	0.52±0.02	1.67±0.14	5.75±1.24
SDSS J0843+3549	20	10.89±0.58	12.07±1.26	13.94±0.98	6.11±1.83	7.04±2.11	30.27±9.08	121.63±1.47
SDSS J0843+2944	7	0.38±0.11	<0.54	0.83±0.23	1.41±0.02	2.22±0.03	5.95±0.18	16.65±1.89
SDSS J0848+0136	7	<0.82	<0.87	<0.98	0.28±0.02	0.20±0.02	<0.41	<3.25
SDSS J0850+3039	7	<0.48	<0.73	0.76±0.24	0.65±0.01	1.13±0.03	6.67±0.18	26.28±1.30
SDSS J0858+3121	7	0.72±0.13	0.88±0.20	1.45±0.25	3.30±0.01	6.19±0.03	27.08±0.22	85.54±1.51
SDSS J0907+5211	20	2.44±0.62	4.36±0.89	4.34±0.94	1.86±0.01	1.69±0.02	8.62±0.12	30.21±1.10
SDSS J0918+2357	7	<0.37	<0.59	<0.64	0.11±0.01 ^a	0.23±0.02	2.13±0.16	10.14±1.85
SDSS J0926+0724	7	1.02±0.21	1.37±0.27	1.65±0.30	1.15±0.01	1.14±0.02	4.74±0.18	16.57±1.30
SDSS J0936+5924	7	1.48±0.17 ^a	1.84±0.28 ^a	1.63±0.21 ^a	1.12±0.01 ^a	1.00±0.02 ^a	2.37±0.14 ^a	10.01±0.82
SDSS J1002+0551	7	1.19±0.20	<0.84	1.06±0.34	0.75±0.02 ^a	0.59±0.02 ^a	1.47±0.17 ^a	13.12±1.30
SDSS J1022+4734	10	2.08±0.23	1.69±0.44	2.62±0.39	1.11±0.01	0.90±0.02	1.70±0.12 ^a	4.35±1.03
SDSS J1032+4926	20	1.85±0.49	2.60±0.72	2.76±0.85	1.46±0.02	2.14±0.02	7.57±0.14	22.56±0.92
SDSS J1034+6001	20	13.82±0.50	17.19±0.78	16.54±0.92	10.56±3.17	17.20±5.16	89.25±26.77	378.75±1.30
SDSS J1040+4745	7	<0.44	<0.69	<0.68	0.66±0.01	0.76±0.02	5.73±0.14	35.45±1.12
SDSS J1044+3008	7	<0.42	<0.69	<0.68	0.30±0.01 ^a	0.39±0.02 ^a	1.81±0.17	9.41±1.39
SDSS J1052+0609	20	5.26±0.77	5.46±0.99	6.55±1.23	2.96±0.02	3.18±0.03	22.16±0.19	84.90±1.70
SDSS J1100+0846	20	4.73±0.79	6.68±1.34	7.66±1.41	15.50±0.02	34.11±0.03	181.77±0.18	543.92±1.39
SDSS J1100+4951	10	2.33±0.22	1.66±0.34	3.25±0.35	1.16±0.01	0.89±0.02	1.76±0.13	4.34±0.95
SDSS J1101+4004	7	<0.40	<0.62	<0.66	0.22±0.01 ^a	0.40±0.02	3.07±0.16	19.99±1.16
SDSS J1102+6459	20	5.27±0.49	7.01±0.90	6.11±0.79	6.86±0.01	11.84±0.02	44.68±0.13	187.79±0.80
SDSS J1109+2659	7	0.39±0.12	<0.49	<0.66	0.38±0.01	0.42±0.02	4.12±0.15	19.66±1.14
SDSS J1109+4233	7	0.52±0.14	0.82±0.20	0.90±0.22	0.76±0.01	1.51±0.02	12.96±0.13	78.13±0.82
SDSS J1110+5848	7	<0.48	<0.88	<0.76	0.44±0.01	1.21±0.02	5.61±0.12	22.30±0.78
SDSS J1111-0053	20	6.12±0.59 ^a	8.26±0.71 ^a	7.99±1.20 ^a	7.02±0.02	7.68±0.03	25.87±0.16	132.89±0.99
SDSS J1123+3105	7	0.64±0.13	0.76±0.20	0.70±0.23	0.53±0.01	0.42±0.02	1.71±0.16	8.96±1.48

Table 2 continued

Table 2 (continued)

Object	$r_{2\text{MASS}}$	F_J	F_H	F_{K_s}	F_{W1}	F_{W2}	F_{W3}	F_{W4}
	($''$)	(mJy)	(mJy)	(mJy)	(mJy)	(mJy)	(mJy)	(mJy)
(1)	(2)	(3)	(4)	(5)	(6)	(7)	(8)	(9)
SDSS J1137+5731	7	<0.38	<0.60	<0.61	0.34±0.01	0.64±0.02	3.19±0.12	11.91±1.12
SDSS J1145+0241	7	1.83±0.21	1.88±0.27	2.17±0.36	1.13±0.02	0.93±0.03	3.92±0.16	11.72±1.28
SDSS J1151+0049	7	0.66±0.20	0.95±0.29	1.49±0.35	0.89±0.02	1.03±0.02	3.90±0.16	15.14±1.07
SDSS J1152+1016	10	3.58±0.33	4.46±0.39	3.72±0.55	3.25±0.01	5.52±0.02	32.88±0.14	125.81±1.11
SDSS J1153+5806	10	2.83±0.21	3.04±0.32	2.58±0.39	2.32±0.01	3.44±0.02	24.76±0.13	98.23±0.94
SDSS J1200+3147	20	2.57±0.47	2.73±0.76	3.19±0.85	2.37±0.01	4.60±0.02	29.89±0.15	138.48±1.04
SDSS J1218+0222	7	0.89±0.18	1.21±0.23	1.79±0.34	0.70±0.01 ^a	0.92±0.03	4.50±0.45	22.44±2.68
SDSS J1230+3943	7	<0.42	<0.71	<0.79	0.23±0.01	0.47±0.02	3.10±0.13	13.46±1.01
SDSS J1238+0927	20	5.66±0.73 ^a	8.71±1.29 ^a	5.05±1.33 ^a	4.89±0.03	6.71±0.03	33.21±0.17	134.24±1.64
SDSS J1238+6703	10	1.17±0.24	1.33±0.41	1.47±0.42	0.73±0.01	0.64±0.02	3.82±0.13	11.49±0.76
SDSS J1240+3534	7	1.18±0.16	0.76±0.23	2.17±0.29	1.10±0.02	1.66±0.02	9.97±0.13	47.66±1.03
SDSS J1258+5239	20	7.51±0.68	10.36±1.11	8.33±0.95	4.26±1.28	4.86±1.46	27.48±8.24	97.84±0.96
SDSS J1300+5454	20	3.04±0.64	3.99±1.11	4.69±1.21	1.64±0.01	1.66±0.02	8.36±0.11	48.03±0.95
SDSS J1316+4452	20	4.21±0.67	7.99±1.17	14.03±1.04	31.02±0.01	50.41±0.02	163.84±0.11	440.10±1.04
SDSS J1323+6104	20	3.98±0.59	5.62±0.94	4.01±0.80	3.83±0.01 ^a	5.82±0.02	28.04±0.11	83.56±1.16
SDSS J1323-0159	7	<0.44	<0.65	<0.90	0.22±0.01 ^a	0.45±0.02	2.89±0.14	13.25±0.88
SDSS J1332+4632	7	<0.49	<0.69	<0.79	0.20±0.02	0.29±0.02	1.55±0.12	9.22±1.08
SDSS J1335+6316	7	0.87±0.16	1.41±0.27	1.03±0.26	0.88±0.01	1.29±0.01	8.54±0.07	45.00±0.66
SDSS J1348+5130	7	<0.47	<0.69	<0.85	0.13±0.01	0.14±0.02	<0.32	<2.23
SDSS J1356+0132	7	1.07±0.21	0.93±0.24	1.29±0.37	1.12±0.01	1.50±0.02	7.53±0.13	29.90±0.74
SDSS J1356+4304	7	<0.46	<0.64	<0.84	0.30±0.01	0.43±0.02	2.11±0.10	8.36±1.05
SDSS J1356+1026	20	4.14±0.68	4.01±0.97	5.05±1.27	2.49±0.01	4.72±0.02	28.35±0.10	203.20±0.80
SDSS J1356+4259	7	0.94±0.15	1.11±0.23	0.98±0.27	0.84±0.01	1.03±0.02	5.44±0.10	25.99±0.81
SDSS J1358+4741	20	3.86±0.56 ^a	3.92±0.82 ^a	5.25±0.97 ^a	2.29±0.01 ^a	1.64±0.01 ^a	10.00±0.12	42.98±0.81
SDSS J1405+4026	10	2.08±0.22	2.41±0.29	3.04±0.32	3.22±0.01	6.55±0.02	43.11±0.12	197.57±0.89
SDSS J1407+5851	7	0.98±0.15	1.60±0.24	1.33±0.24	0.82±0.02	0.75±0.02	2.76±0.12	9.99±0.92
SDSS J1413-0142	7	<0.53	<0.74	<1.00	0.18±0.01	0.20±0.02	2.44±0.16	17.31±0.92
SDSS J1430+1339	20	5.91±0.45	8.13±0.80	7.16±0.99	6.87±0.02	11.19±0.02	41.21±0.10	187.04±0.67
SDSS J1437+3011	20	5.71±0.61 ^a	5.33±0.99 ^a	5.75±0.86 ^a	3.63±0.03	4.13±0.03	16.57±0.10	90.25±0.80
SDSS J1450-0106	7	2.02±0.22	2.06±0.29	2.23±0.34	1.60±0.01	1.90±0.02	7.49±0.12	27.72±1.01
SDSS J1455+3226	15	1.81±0.36	<1.76	<1.85	1.35±0.01	1.54±0.02	10.80±0.09	40.81±0.87
SDSS J1513+4319	7	1.35±0.18	<0.90	1.83±0.33	1.28±0.01	1.74±0.02	8.19±0.08	30.15±0.47
SDSS J1552+2753	20	4.68±0.58 ^a	6.59±0.81 ^a	4.38±0.88	2.89±0.87	3.24±0.97	16.22±4.87	61.91±0.69
SDSS J1558+3513	10	1.56±0.19	1.82±0.31	2.04±0.35	0.81±0.01	0.98±0.02	6.96±0.09	31.76±0.69
SDSS J1605+0742	7	<0.54	0.88±0.27	<1.04	0.31±0.02 ^a	0.41±0.03	2.96±0.14	18.60±1.26
SDSS J1616+4321	7	0.75±0.16	<0.85	1.35±0.29	0.63±0.01	0.77±0.02	3.72±0.08	21.08±0.51
SDSS J1624+3344	7	1.03±0.13 ^a	1.31±0.19 ^a	1.34±0.22 ^a	1.52±0.01 ^a	2.29±0.02 ^a	12.52±0.12	57.79±0.79
SDSS J1641+4321	7	0.65±0.18	0.78±0.25	1.59±0.29	2.24±0.01	3.93±0.02	14.65±0.11	48.98±1.25
SDSS J2133+1009	10	2.76±0.26	2.99±0.44	2.65±0.43	1.59±0.02	1.33±0.02	5.75±0.15	25.11±1.23
SDSS J2134-0749	10	1.55±0.29	1.50±0.42	<1.70	0.99±0.02	1.33±0.03	9.45±0.22	33.64±1.95
SDSS J2144-0810	7	0.62±0.16 ^a	0.97±0.25 ^a	<0.93 ^a	0.46±0.02 ^a	0.37±0.02 ^a	1.28±0.20	<5.05

^a The flux density is measured after GALFIT decomposition.

NOTE— (1) Source name. (2) The aperture radius of 2MASS aperture photometry. (3) The flux density and 1σ uncertainty at J band. (4) The flux density and 1σ uncertainty at H band. (5) The flux density and 1σ uncertainty at K_s band. (6) The flux density and 1σ uncertainty at $W1$ band. (7) The flux density and 1σ uncertainty at $W2$ band. (8) The flux density and 1σ uncertainty at $W3$ band. (9) The flux density and 1σ uncertainty at $W4$ band. The objects fainter than 3σ of the sky variation are replaced by the 3σ as upper limits.

Table 3. *Herchel* Photometry of Type 2 Quasars

Object	Aperture	F_{70}	F_{100}	F_{160}	F_{250}	F_{350}	F_{500}
		(mJy)	(mJy)	(mJy)	(mJy)	(mJy)	(mJy)
(1)	(2)	(3)	(4)	(5)	(6)	(7)	(8)
SDSS J0041-0952	l	31.40±3.90	67.53±5.44	62.87±16.23	29.31±9.39	<24.60	<33.61
SDSS J0119-1026	s	54.04±3.17	61.76±3.66	74.22±5.31	<32.98	<25.98	<31.67
SDSS J0202+1247	l	236.06±4.33	301.05±7.06	347.36±26.11	161.56±10.57	88.33±8.94	34.01±10.71
SDSS J0339-0548	s	85.99±2.59	111.50±3.52	108.10±8.11	57.71±10.46	<24.99	<31.78
SDSS J0747+3200	s	74.81±2.24	115.78±3.06	123.59±8.14	73.17±10.07	29.74±9.15	<33.15
SDSS J0752+2510	s	81.89±2.71	89.71±3.23	99.05±9.55	46.85±11.49	<29.44	<45.48
SDSS J0753+3847 ^a	e	127.22±5.32	158.53±10.07	202.09±34.62	80.86±11.63 ^c	55.08±9.11 ^c	<33.50
SDSS J0753+2309	s	26.11±2.46	21.91±2.50	<32.93	<32.20	<25.75	<30.95
SDSS J0759+5050	l	755.97±4.45	690.89±7.74	428.72±21.97	182.44±11.15	43.71±9.01	<36.26
SDSS J0802+2552	l	477.56±4.59	390.79±5.38	266.35±19.69	77.70±10.69	<26.57	<33.45
SDSS J0802+3046	s	78.21±2.24	85.54±3.50	71.86±10.61	37.59±10.36	<25.91	<33.88
SDSS J0803+3926	e	216.86±6.32	209.06±6.72	167.36±18.80	66.04±11.74	45.28±9.12	<32.59
SDSS J0805+2818	l	301.66±5.49	404.84±4.56	387.37±30.60	169.85±9.85	70.53±8.62	<30.40
SDSS J0811+4442	s	104.30±2.79	156.64±3.28	202.63±8.73	116.98±9.72	63.17±8.69	<33.27
SDSS J0818+3604	s	92.21±2.47	75.37±2.90	50.00±10.56	<31.21	<26.70	<35.98
SDSS J0823+3132	s	21.28±3.64	13.08±2.95	<24.58	<31.55	<26.11	<35.50
SDSS J0825+2025	s	<6.48	10.46±2.17	<25.60	<32.30	<28.70	<33.38
SDSS J0835+5240	l	365.14±5.09	375.46±7.29	380.51±21.14	160.90±10.65	80.68±9.41	38.70±11.74
SDSS J0840+3320	s	54.92±2.57	56.05±2.61	83.49±9.53	50.70±10.01	<30.13	<36.34
SDSS J0841+0334	s	10.57±3.08	<8.55	<22.50	<29.76	<25.38	<34.15
SDSS J0843+3549	l	267.70±3.61	292.02±5.92	318.73±13.50	121.78±10.46	49.64±9.22	<35.05
SDSS J0843+2944	s	<6.80	15.73±2.75	<27.08	<19.65	<22.02	<27.12
SDSS J0848+0136	s	<11.20	9.76±2.87	<22.31	<33.38	<29.02	<36.26
SDSS J0850+3039	s	28.02±3.04	23.31±2.71	<32.43	<32.11	<29.60	<34.14
SDSS J0858+3121	l	79.73±5.04	71.43±7.60	60.34±18.30	<31.41	<27.65	<32.23
SDSS J0907+5211	s	86.67±1.85	105.93±1.77	113.70±7.09	49.42±10.01	<26.43	<34.07
SDSS J0918+2357	s	12.93±2.80	<11.75	<29.34	<32.88	<31.15	<33.09
SDSS J0926+0724	s	54.54±3.04	97.39±3.48	133.52±11.15	76.94±9.89	43.34±7.90	<30.82
SDSS J0936+5924 ^a	l	26.59±5.33	<16.87	<47.80	<44.37	<33.63	<31.08
SDSS J1002+0551 ^b	s	47.67±3.24	50.73±3.00	54.43±12.64	<35.01	<27.41	<32.03
SDSS J1022+4734 ^b	s	16.18±2.74	26.80±3.07	42.51±9.14	<34.03	<28.19	<34.24
SDSS J1032+4926	s	25.59±2.87	37.27±3.39	<29.47	<30.74	<29.58	<34.56
SDSS J1034+6001	e	885.02±4.62	951.28±6.26	742.88±27.90	273.50±15.20	133.34±13.84	63.36±15.91
SDSS J1040+4745	l	364.77±6.63	415.78±4.33	339.57±16.82	136.69±10.58	60.47±8.17	<34.39
SDSS J1044+3008	s	21.23±2.33	17.75±3.37	33.23±6.47	<31.93	<26.82	<35.80
SDSS J1052+0609	l	248.40±4.36	275.11±4.69	295.29±29.25	118.28±11.86	56.93±8.85	39.97±11.42
SDSS J1100+0846	l	601.62±6.42	594.15±7.67	482.42±19.46	207.06±11.20	74.63±8.28	<34.37
SDSS J1100+4951	s	10.95±2.62	23.36±3.99	37.89±9.12	<31.91	<27.54	<38.91
SDSS J1101+4004 ^b	s	51.12±2.57	38.85±3.96	29.84±9.38	<31.16	<27.49	<35.33
SDSS J1102+6459	l	594.71±5.52	581.01±6.86	449.03±15.92	161.08±11.37	46.22±9.24 ^c	<33.94
SDSS J1109+2659	s	129.07±2.96	174.26±3.05	165.96±7.40	102.22±11.28	50.04±9.41	<31.75
SDSS J1109+4233	l	505.62±4.57	576.02±6.02	421.75±24.85	172.28±10.29 ^c	74.08±9.10 ^c	51.02±11.87 ^c
SDSS J1110+5848	s	33.23±3.18	21.73±3.42	<32.23	49.07±10.05	28.23±9.03	<33.28
SDSS J1111-0053	l	825.92±4.44	927.79±6.49	681.94±28.11	253.13±10.69	96.03±9.43	<37.46
SDSS J1123+3105	s	42.81±1.86	67.02±2.34	73.48±11.06	49.39±11.18	<26.71	<34.51
SDSS J1137+5731	s	19.54±2.52	27.98±5.34	<34.70	<30.16	<29.55	<35.96

Table 3 continued

Table 3 (continued)

Object	Aperture	F_{70}	F_{100}	F_{160}	F_{250}	F_{350}	F_{500}
(1)	(2)	(mJy)	(mJy)	(mJy)	(mJy)	(mJy)	(mJy)
(1)	(2)	(3)	(4)	(5)	(6)	(7)	(8)
SDSS J1145+0241	s	49.34±3.36	60.87±2.52	97.45±7.62	55.87±11.20	47.07±9.10	<32.77
SDSS J1151+0049	s	10.16±2.68	<9.73	<42.59	<31.91	<25.64	<30.32
SDSS J1152+1016	l	152.31±3.57	128.83±5.59	82.75±17.31	<29.18	<27.84	<31.50
SDSS J1153+5806	l	250.56±5.65	272.21±6.76	229.88±20.86	98.48±10.02	37.35±10.33	<36.01
SDSS J1200+3147	e	165.42±7.65	142.55±8.83	111.18±35.20	40.72±10.47	<27.15	<31.41
SDSS J1218+0222	s	112.85±3.65	143.43±5.34	125.57±11.83	58.70±6.00
SDSS J1230+3943	s	11.64±2.64	16.44±3.80	27.78±8.60	<30.67	<26.01	<32.37
SDSS J1238+0927	l	118.16±3.79	131.18±8.80	138.05±12.76	50.06±10.80	<29.11	<33.42
SDSS J1238+6703	s	62.37±3.46	100.53±4.75	180.27±17.85	71.17±10.96	55.55±9.91	<34.13
SDSS J1240+3534	l	244.28±5.12	313.29±7.26	262.71±22.43	102.10±11.00	<27.81	<34.32
SDSS J1258+5239	l	71.07±4.02	123.18±5.85	201.48±22.86	75.21±11.32	47.46±9.15 ^c	<32.68
SDSS J1300+5454	s	93.82±2.11	82.06±2.61	62.80±8.71	<33.41	<25.95	<37.55
SDSS J1316+4452	l	761.31±3.84	835.05±6.78	676.80±25.08	285.76±10.98	105.60±10.45	35.77±11.09
SDSS J1323+6104	s	81.67±3.55	74.91±3.56	85.06±9.88	45.91±10.30	<25.76	<37.28
SDSS J1323-0159	s	33.15±2.56	36.31±3.03	38.12±6.02	<31.27	<24.95	<32.93
SDSS J1332+4632	s	28.05±3.60	33.17±3.24	<24.70	<35.99	<29.05	<36.15
SDSS J1335+6316	l	195.69±5.09	203.49±5.39	139.64±19.68	57.91±10.17	<29.35	<34.01
SDSS J1348+5130	s	12.22±1.69	15.75±4.36	31.38±9.51	38.76±10.07	36.96±9.56	<31.07
SDSS J1356+0132	s	116.43±2.15	142.01±2.65	145.04±13.78	58.31±10.74	<27.17	<33.01
SDSS J1356+4304 ^a	s	11.41±2.57	6.48±1.98	<22.13	<31.37	<26.24	<33.38
SDSS J1356+1026	l	796.15±5.83	680.03±6.53	399.90±32.93	135.94±10.51	48.38±9.44 ^c	<30.08
SDSS J1356+4259 ^b	s	94.40±3.52	97.42±1.72	87.02±10.60	45.56±11.36 ^c	<28.24	<35.20
SDSS J1358+4741	l	229.68±4.58	266.43±5.89	254.53±30.70	98.35±12.50 ^c	48.00±11.64 ^c	35.70±11.52 ^c
SDSS J1405+4026 ^b	l	232.81±4.72	208.46±5.89	176.44±20.90	58.79±10.91 ^c	<26.60	<32.60
SDSS J1407+5851	s	56.56±3.42	70.54±3.87	98.16±8.59	57.59±10.75	32.26±9.18	<39.23
SDSS J1413-0142	s	116.73±3.41	133.30±4.53	103.75±13.62	39.49±10.68	<27.97	<35.86
SDSS J1430+1339	e	399.43±7.94	453.37±9.30	352.56±38.89	115.02±11.14	49.47±9.37	<33.22
SDSS J1437+3011	l	230.20±4.32	222.52±7.02	173.36±15.36	85.99±10.83	<28.36	<34.75
SDSS J1450-0106 ^b	s	43.31±3.40	47.39±3.06	65.08±12.16	<32.65	<28.97	<33.52
SDSS J1455+3226	s	63.44±2.35	76.53±3.23	95.45±5.76	55.81±10.13	<26.17	<32.52
SDSS J1513+4319	s	77.63±3.37	109.95±3.99	131.28±16.68	73.26±10.29	30.60±9.40	<33.46
SDSS J1552+2753	l	127.22±6.58	127.84±5.91	167.01±21.62	54.57±11.20	37.39±9.48	<35.31
SDSS J1558+3513	s	54.84±2.82	60.38±3.97	69.66±8.05	<33.00	<27.73	<32.68
SDSS J1605+0742 ^b	s	50.95±2.89	52.88±4.28	37.33±7.82	<31.95	<28.93	<34.01
SDSS J1616+4321	s	72.13±1.92	67.29±3.85	61.59±6.39	<32.50	<28.42	<32.55
SDSS J1624+3344	s	70.71±2.82	75.87±4.21	75.59±11.73	<34.74	<26.38	<37.20
SDSS J1641+4321	s	60.43±2.81	74.76±3.11	51.45±8.51	41.26±10.42	<27.96	<36.72
SDSS J2133+1009	l	104.94±4.46	162.08±8.00	188.14±10.06	96.12±10.62	29.88±9.82	<36.93
SDSS J2134-0749	s	54.94±2.25	52.65±3.40	44.68±10.25	<31.37	<27.04	<32.89
SDSS J2144-0810	s	12.41±2.02	24.67±4.50	49.73±12.69	<34.85	<30.94	<32.27

^a All the bands are > 5% affected by the contamination.

^b The 160 μm band is > 5% affected by the contamination.

^c The measurement may be contaminated. Since the companions are always much fainter than the quasar in PACS maps, we believe that the contamination is not significant.

NOTE— (1) Source name. (2) The aperture type adopted to extract the flux. “s”, “l”, and “e” refer to small, large, and extended apertures, respectively. (3) The flux density and 1σ uncertainty at 70 μm . (4) The flux density and 1σ uncertainty at 100 μm . (5) The flux density and 1σ uncertainty at 160 μm . (6) The flux density and 1σ uncertainty at 250 μm . (7) The flux density and 1σ uncertainty at 350 μm . (8) The flux density and 1σ uncertainty at 500 μm . The objects fainter than 3σ of the sky variation are replaced by the 3σ as upper limits.

Table 4. Model Parameters and Priors

Models	Parameters	Units	Discreteness	Priors	Descriptions
(1)	(2)	(3)	(4)	(5)	(6)
BC03	M_*	M_\odot	✗	$[10^6, 10^{14}]$	Stellar mass.
	t	Gyr	✓	5 (fixed)	The age of the single stellar population.
CAT3D	i	–	✓	[0.0, 90.0]	The inclination angle of the torus.
	a	–	✓	[-2.5, -0.25]	The power-law index of the dust cloud radial distribution.
	N_0	–	✓	[5.0, 10.0]	The number of dust clouds along an equatorial line-of-sight.
	h	–	✓	[0.25, 1.50]	The dimensionless scale height of the vertical Gaussian distribution of the dust cloud.
	L	erg s^{-1}	✗	$[10^{40}, 10^{50}]$	Torus luminosity.
DL07	U_{\min}	–	✓	[0.10, 25.0]	The minimum intensity of the interstellar radiation field (ISRF).
	U_{\max}	–	✓	10^6 (fixed)	The maximum intensity of the ISRF for the dust in photo-dissociation region (PDR).
	α	–	✗	2 (fixed)	The power-law index of the intensity distribution of the ISRF.
	q_{PAH}	–	✓	0.47 (fixed)	The mass fraction of the PAH molecules among the total dust.
	γ	–	✗	0.03 (fixed)	The mass fraction of the PDR dust component.
	M_d	M_\odot	✗	$[10^5, 10^{11}]$	Total dust mass.

NOTE—(1) The name of the models used in the SED fitting. (2) The parameters of each model. (3) The units of the parameters. (4) Whether the parameter is discrete and requires interpolation to implement the MCMC fitting. (5) The prior range of the parameters. (6) A brief description of the parameters.

Table 5. Statistics of dust, gas, and stellar masses

Kaplan-Meier estimator			
	$\log M_d$	$\log M_{\text{gas}}$	$\log M_*$
	(M_\odot)	(M_\odot)	(M_\odot)
Type 1 quasar	$7.72^{+0.32}_{-0.31}$	$9.82^{+0.32}_{-0.32}$	$10.90^{+0.24}_{-0.18}$
Type 2 quasar	$7.74^{+0.36}_{-0.28}$	$9.82^{+0.36}_{-0.29}$	$10.93^{+0.19}_{-0.25}$
Monte Carlo method			
	$\log M_d$	$\log M_{\text{gas}}$	$\log M_*$
	(M_\odot)	(M_\odot)	(M_\odot)
Type 1 quasar	$7.69^{+0.04}_{-0.04}$	$9.78^{+0.07}_{-0.05}$	$10.92^{+0.04}_{-0.05}$
Type 2 quasar	$7.76^{+0.04}_{-0.04}$	$9.83^{+0.06}_{-0.05}$	$10.88^{+0.04}_{-0.05}$

NOTE— Upper part: The 50^{+25}_{-25} th percentiles of the dust, gas, and stellar masses are calculated with the Kaplan-Meier estimator. Lower part: The 50^{+25}_{-25} th percentiles of the median values are calculated using a Monte Carlo method to resample the data based on the measurement and uncertainty of each object, assuming a Gaussian distribution; the median of each quantity is obtained using the Kaplan-Meier estimator.